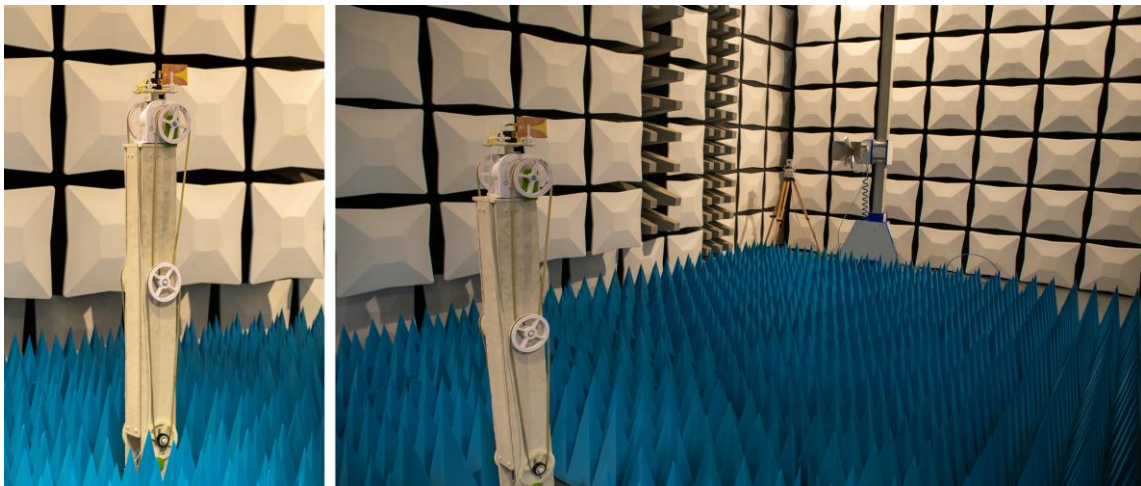




Master thesis

Degree of Master of Science in Engineering,
Electrical Engineering, 300 credits



Bladder Monitoring Using Ultra-Wideband Radar and
Vivaldi Antenna

Electrical Engineering, 30 credits

Halmstad, 2023-05-23

Erica Jonsson & Attila Kovács

Bladder Monitoring Using Ultra-Wideband Radar and Vivaldi Antenna
Erica Jonsson
Attila Kovacs
© Copyright Erica Jonsson & Attila Kovacs, 2023. All rights reserved.

Preface

We would like to start this report by stating that this thesis is solely based on our original idea and has not been influenced or derived from any external company. We would also like to thank our supervisors, Ross Friel, Maria De Lauretis, and Per Sandrup, for their feedback and encouragement.

Erica Jonsson & Attila Kovács

Halmstad, Sweden

May 23, 2023

Abstract

Millions worldwide cannot tell when their bladder is nearing total capacity. The catheter, a tube to empty the bladder, is a vital part of life for many people. A catheter is, however, not a comfortable option, and it is the most common cause of infection in people staying in hospitals. This thesis aims to make the process more comfortable and non-invasive. The proposed idea is to use a UWB radar system with Vivaldi antennas to monitor the bladder state. Research shows that UWB radars can see a difference between a full and an empty phantom bladder.

However, current research that explores the usage of UWB radar systems to monitor the bladder state does not consider regulations other than the ones set by FCC. They also only perform experiments on a phantom bladder. This thesis investigates the practical viability of using a UWB radar system designed per the restricted regulations set by Post- och Telestyrelsen. The thesis includes the design, simulations, manufacturing, and testing of the antennas as well as the radar system. The goal was to test the system in both simulations, with a phantom model and with a human body as a target, to advance the current state of research and determine its practicality for real-life applications. The simulations showed a significant difference in reflections between full and empty bladders. The measurements from the experiments showed a slight difference in amplitude as well, although not as great as predicted due to a longer pulse. The Vivaldi antennas performed as expected according to both theory and simulations and they should work as desired in further experiments that use a UWB radar to monitor the bladder state per the PTS regulations.

This thesis is solely based on an original idea and has not been influenced or derived from any external company.

Contents

1	Introduction	1
1.1	Research Questions.....	2
1.2	Contributions	3
1.3	Limitations	3
2	Background.....	5
2.1	Bladder-scanning today.....	5
2.2	Ultra-wideband (UWB)	5
2.3	Ultra-wideband as a bladder scanner	6
2.4	Phantom Model.....	8
2.5	Antenna Design.....	9
2.5.1	Tapered Slot Antennas	9
2.5.2	Antenna Feed.....	10
2.5.3	Impedance matching.....	11
2.6	EM simulations.....	12
2.7	Radar design.....	12
2.7.1	Signal processing	13
3	Methods.....	15
3.1	Antenna Design.....	15
3.1.1	Impedance matching	16
3.1.2	Construction in ADS.....	17
3.2	Fabrication of the antenna	18
3.3	Antenna characterization	19
3.4	Simulations in EMPro	22
3.4.1	EMPro simulation specifications.....	23
3.5	Radar design.....	24
3.5.1	Phantom model	25
3.6	Experiments.....	26
4	Results	29
4.1	Antenna design	29
4.2	Radar	33
4.3	Simulations	35
5	Discussion	39
5.1	Antenna	39
5.2	Radar	40
5.3	Addressing the research questions	41
5.4	Further works	42
5.5	Social aspect.....	43
6	Conclusions.....	45

List of Figures

FIGURE 1: SIMPLIFIED MODEL OF DIFFERENT BODY LAYERS WITH DIFFERENT RELATIVE PERMITTIVITY AND THE SUPPOSED REFLECTIONS OF THE TRANSMITTING ANTENNAS (TX) SIGNAL BEING PICKED UP BY THE RECEIVING ANTENNA RX. THE IMAGE DOES NOT REPRESENT THE THICKNESSES OF THE DIFFERENT LAYERS.	7
FIGURE 2: DIAGRAM OF A FULL BLADDER PHANTOM MODEL (MUSCLE-URINE-MUSCLE).	9
FIGURE 3: MICROSTRIP-TO-SLOTLINE TRANSITION WITH QUARTER-WAVELENGTH RADIAL STUBS ORTHOGONAL TO EACH OTHER.	11
FIGURE 4: THE DESIGNED ANTENNAS TAPERED-SHAPED FEEDING LINE.	17
FIGURE 5: ANTENNA LAYOUT IN ADS STRICTLY DESIGNED ACCORDING TO THEORY.	17
FIGURE 6: THE ADDED OFFSET OF 5.35 MM ON THE EDGE OF THE ANTENNA'S TAPERED SLOT TO INCREASE PERFORMANCE.	18
FIGURE 7: THE ANTENNAS WITH THE ATTACHED BOXES FITTED ON THE PLATE THAT ENABLES HORIZONTAL MOVEMENT.	19
FIGURE 8: MEASURED $S(1,1)$ PARAMETER FOR THE TRANSMITTING ANTENNA USING A NETWORK ANALYZER.	20
FIGURE 9: MEASURED AND SIMULATED RECEIVED POWER IN DBM EVERY 5° WHEN THE ANTENNAS ARE SEPARATED WITH 3 M AND A TRANSMITTED SIGNAL OF 3.95 GHz WITH A TRANSMIT POWER OF 0.001 W.	21
FIGURE 10: SETUP IN THE ANECHOIC CHAMBER WHEN MEASURING THE ANTENNAS RADIATION.	21
FIGURE 11: THE SETUP IN EMPro WITH THE ANTENNAS IMPORTED FROM ADS AND THE FULL PHANTOM MODEL IN THE SAME DESIGN AS THE 3D-PRINTED ONE USED IN THE EXPERIMENTS.	22
FIGURE 12: SIMULATION SETUP WITH A TRANSMITTING AND A RECEIVING ANTENNA IMPORTED FROM ADS, AND A SIMPLIFIED MODEL OF THE HUMAN TORSO WITH A FULL BLADDER TO THE RIGHT AND AN EMPTY BLADDER TO THE LEFT. THE RED PART IS SKIN AND HAS A THICKNESS OF 10 MM, THE GREEN PART IS FAT AND HAS A THICKNESS OF 90 MM, THE ORANGE PART IS MUSCLE WITH A THICKNESS OF 150 MM, AND THE YELLOW PART IS THE BLADDER WALLS. THE FULL BLADDER CONTAINS URINE (IN BLUE), AND IT HAS A RADIUS OF 4 CM. THE EMPTY BLADDER IS SMALLER AND DOES NOT CONTAIN URINE.	22
FIGURE 13: THE UPPER DIAGRAM SHOWS THE FREQUENCY RESPONSE OF THE GAUSSIAN FIRST ORDER DERIVATIVE WITH PULSE WIDTH 0.25 NS, AND THE BOTTOM ONE HAS A PULSE WIDTH OF 10 NS.	23
FIGURE 14: WAVEFORM OF THE GENERATED PULSE WITH A PULSE WIDTH OF 10 NS.	24
FIGURE 15: LAYOUT OF THE RADAR SYSTEM WITH A TRIGGER, PULSE GENERATOR, OSCILLOSCOPE, TWO ANTENNAS, AND THE TARGET.	25
FIGURE 16: LAYOUT OF THE PHANTOM MODEL OF A FULL BLADDER.	26
FIGURE 17: LAYOUT OF THE PHANTOM MODEL OF AN EMPTY BLADDER.	26
FIGURE 18: SETUP FOR MEASUREMENTS IN THE ANECHOIC CHAMBER WITH A PHANTOM MODEL 30 CM FROM THE ANTENNAS.	27
FIGURE 19: LAYOUT OF THE FINAL ANTENNA DESIGN CONSTRUCTED IN ADS.	29
FIGURE 20: THE TOP LAYER OF THE ANTENNA IS TO THE LEFT, AND THE BOTTOM LAYER IS TO THE RIGHT.	30
FIGURE 21: THE S_{11} PARAMETERS OF THE ANTENNA BEFORE AND AFTER ITERATION FOR THE FREQUENCY RANGE 3.1 - 4.8 GHz WITH A MARKER AT THE REFLECTION COEFFICIENT MINIMUM AND THE CORRESPONDING PHASE.	30
FIGURE 22: RADIATION PATTERN AT 3.1 GHz, 3.95 GHz, AND 4.8 GHz AFTER ITERATIONS.	31
FIGURE 23: THE VIVALDI ANTENNAS RADIATION PATTERN MEASURED IN AN ANECHOIC CHAMBER.	31
FIGURE 24: VSWR OF THE FABRICATED ANTENNA MEASURED WITH A NETWORK ANALYZER COMPARED TO THE VSWR OF THE FINAL AND INITIAL ANTENNA DESIGNS IN ADS FOR THE FREQUENCY RANGE 3.1-4.8 GHz.	32
FIGURE 25: SMITH CHART REPRESENTATION OF THE REFLECTION COEFFICIENT. THE IMPEDANCE FOR THE FINAL DESIGN IS $Z = 52.65 - j4.75 \Omega$ AT 4 GHz.	32
FIGURE 26: EQUIVALENT CIRCUIT OF MICROSTRIP FEED AFTER ALTERATIONS AND THE CORRESPONDING MICROSTRIP GEOMETRIES.	33
FIGURE 27: THE RECEIVED SIGNAL FROM MEASUREMENTS WITH EMPTY AND FULL PHANTOM MODELS, AND NO TRANSMISSION. THE DATA HAS EXPONENTIAL SMOOTHING WITH $\alpha = 0.99$.	33
FIGURE 28: RECEIVED SIGNAL (AFTER FFT AND EXPONENTIAL SMOOTHING) COMPARED TO THE 10 NS PULSE FREQUENCY RESPONSE MEASURED WITH THE OSCILLOSCOPE DIRECTLY FROM THE PULSE GENERATOR.	34

FIGURE 29: THE MEASURED RESULTS FROM ALTERING THE DISTANCE BETWEEN THE TRANSMITTING AND RECEIVING ANTENNAS WITH DISTANCES 4, 6, 8, AND 10 CM	34
FIGURE 30: MEASUREMENTS FROM EXPERIMENTS WITH THE HUMAN BODY. THE BLUE LINE SHOWS THE MEASUREMENTS POST-VOIDING, AND THE RED LINE SHOWS THE MEASUREMENTS PRE-VOIDING.....	35
FIGURE 31: $S(2,1)$ FROM SIMULATIONS IN EMPro WITH THE SETUP USING THE PULSE AND PHANTOM MODEL USED IN REAL-LIFE EXPERIMENTS. THE GRAPH INCLUDES FULL AND EMPTY BLADDER AS WELL AS NO TARGET.	36
FIGURE 32: RESULTS FROM THE SIMULATIONS WITH A PHANTOM TORSO. THE RED LINE IS WITH A FULL BLADDER, THE BLUE LINE IS WITH AN EMPTY BLADDER, AND THE YELLOW LINE IS WITHOUT ANY TARGET IN FRONT OF THE ANTENNAS.....	36
FIGURE 33: ABSOLUTE VALUE OF THE DIFFERENCE BETWEEN FULL AND EMPTY BLADDER.	37
FIGURE 34: RESULTS FROM SIMULATIONS OF THE FULL BLADDER; THE RED GRAPH SHOWS THE RESULTS FROM HAVING THE ANTENNAS PARALLEL TO EACH OTHER, AND THE BLUE GRAPH SHOWS THE RESULT FROM HAVING THEM ON OPPOSITE SIDES OF THE BODY.....	37
FIGURE 35: SIMULATIONS OF DIFFERENT DISTANCES BETWEEN THE TRANSMITTING AND RECEIVING ANTENNA. THE TRANSMITTING ANTENNA TRANSMITS THE PULSE GENERATED BY THE PULSE GENERATED, WHICH IS IMPORTED TO EMPro, IT IS A SQUARE WAVE WITH A PULSE WIDTH OF 10 NS.	38

List of Tables

TABLE 1: FREQUENCY LIMITS FOR THE ANTENNA BASED ON THE PTS REGULATIONS IN THE EU AND THE CORRESPONDING FREE SPACE WAVELENGTHS.	15
TABLE 2: ANTENNA PARAMETERS BEFORE ITERATION.	17
TABLE 3: ANTENNA PARAMETERS AFTER ITERATIONS AND THE INITIAL PARAMETERS, ALTERED VALUES ARE IN RED.	29

Acronyms & Abbreviations

ADS	ADVANCED DESIGN SYSTEMS
DFT	DISCRETE FOURIER TRANSFORM
EIRP	EFFECTIVE ISOTROPIC RADIATED POWER
FEM	FINITE ELEMENT METHOD
FFT	FAST FOURIER TRANSFORM
FWHM	FULL WIDTH AT HALF MAXIMUM
PRR	PULSE REPETITION RATE
S-PARAMETERS	SCATTERING PARAMETERS
TSA	TAPERED SLOT ANTENNA
UWB	ULTRA-WIDEBAND
VSWR	VOLTAGE STANDING WAVE RATIO

1 Introduction

Millions worldwide cannot tell when their bladder is nearing total capacity. The catheter, a tube to empty the bladder, is a vital part of life for many people. A catheter is, however, not a comfortable option, and it is the most common cause of infection in people staying in hospitals [1]. This thesis aims to design, simulate, manufacture, and test a real-time bladder scanner using radar technology to dignify the process and make it as comfortable as possible. The scanner intends to help notify the user or their caretaker before their bladder is close to reaching total capacity, around 500 ml. As urine flows in, the bladder expands, and for an average healthy person, the urge to urinate occurs at approximately 200-300 ml [2].

An important parameter when designing a radar system is frequency. It must penetrate the body the right amount; too low frequencies have long wavelengths and penetrate deeper into the body tissue, while higher frequencies do not penetrate deep enough [3]. The resolution also depends on the frequency; it is higher with high frequency and lower with low frequency, which results in a trade-off between resolution and penetration depth. Ultra-wideband (UWB) technology can solve the trade-off by offering high resolution and maintaining a suitable penetration depth [4]. Existing studies [5]–[7] scan a phantom model with UWB signals, covering a broad spectrum of frequencies. The UWB technique ranges in frequency from 3.1 to 10.6 GHz in America per regulations imposed by the Federal Communications Commission (FCC) [7]. However, in Sweden, the frequency range is more restricted, and the limits are set to 3.1 to 4.8 and 6 to 8.5 GHz by Post- och telestyrelsen (PTS) [8]. For the frequencies 3.1 to 4.8 GHz, the maximum mean e.i.r.p. (effective isotropic radiated power) spectral density is -41.3 dBm/MHz, and a maximum peak e.i.r.p. of 0 dBm defined in a bandwidth of 50 MHz at the frequency with the highest radiated power average. However, these values are only acceptable if the time for all transmitted signals does not exceed 5% of the time every second and 0.5% of the time every hour. The limit affects the duty cycle of the radar system, and the technique is therefore called Low Duty Cycle (LDC) mitigation technique. In the gap of the frequency range (4.8 – 6 GHz), the signals are limited to a maximum mean e.i.r.p. spectral density of -70 dBm/MHz, and may only be used indoors to protect the radio astronomy services [8].

Another critical part of the radar system is the antenna, and this thesis includes the design process and fabrication of a Vivaldi antenna. The antenna has an exponential taper design that enables a broader bandwidth suitable for UWB applications. Depending on the frequency, different parts of the taper radiate efficiently [9], and the antenna is designed accordingly. The antenna has design goals that it should meet. The goals match the needs of this thesis, and they are as follows:

- VSWR should be lower than 2
- The radiation pattern should be directional
- It should have wideband radiation
- The operating frequency should be the permitted frequency range of 3.1 - 4.8 GHz

The VSWR describes how well the antenna is impedance matched. The limit is usually two, which equals a reflection coefficient of -10 dB [10]. The radiation pattern should have a directional lobe since it should work in one direction and penetrate properly. The antenna should also be wideband to cover all operating frequencies and qualify as a UWB antenna. It should radiate properly for the frequencies 3.1-4.8 GHz, the chosen range according to the PTS-permitted band.

When the bladder is empty, the received signal should show two peaks representing the reflection from the boundary between tissue and the inside of the bladder, i.e., the posterior and anterior bladder walls. When the bladder is full, the first peak should be higher since this represents the reflection of the boundary between tissue and urine [6]. This boundary will show a more extensive reflection since the difference in relative permittivity is great between tissue ($\epsilon_r \approx 20$) and urine ($\epsilon_r = 81$). The goal is to see the difference and find the optimal measurement method regarding positioning the antennas.

The thesis will introduce the essential theory in [2. Background](#) needed to be able to answer the research questions below. Chapter [3. Methods](#) then utilizes the theory and describes how to use the previously presented theory to realize an antenna and a radar system to see urine in a bladder. The findings are then presented in [4. Results](#), which the chapter [5. Discussion](#) examines and [6. Conclusions](#) concludes.

1.1 Research Questions

The research questions that this thesis aims to answer are the following:

- Is it possible to see a difference between empty and full bladder using the antenna designed and fabricated in this thesis and while following the PTS regulations?
- What is the optimal positioning of the transmitting and receiving antennas and their optimal distance to the target for accurate detection?
- How will full 3D simulations of the bladder compare to the experimental data?

1.2 Contributions

As section [2.3 Ultra-wideband as a bladder scanner](#) further discusses, existing research shows that it is possible to detect water accumulation in the human body using UWB. However, previous research absences two things; they only use phantom models to imitate the bladder and surrounding body tissue to prove the theory, and they only consider the FCC regulations. This thesis will start by simulating the scenario with the designed antenna, then performing tests on a phantom model, and lastly, on the human body for a more complex result. The phantom model will verify the theory and our setup, while the human body experiments will provide new knowledge and insights. Furthermore, the setup and antenna design will align with the more restricted regulations in Sweden, which is the same as for most of Europe.

1.3 Limitations

The simulations are also a limitation as they will be ideal. All bodies are different, and the distinct layers of the body, such as fat and muscle, vary from person to person. The body is also constantly changing, and some research shows that the dielectric properties differ with age and other parameters. However, the simulations will be performed in a controlled environment with an ideal body.

PTS limits the emitted power to -41.3 dBm/MHz and the frequency range to 3.1 - 4.8 GHz and 6 - 8.5 GHz. A well-designed antenna with good matching is essential as -41.3 dBm/MHz is relatively low.

2 Background

2.1 Bladder-scanning today

There is already a market for bladder scanners widely used in healthcare, such as ultrasound [11]. However, these are often large and expensive equipment requiring expertise to operate and interpret the information. They are not self-monitoring, and to avoid personnel spending hours operating it, a self-monitoring option is more optimal. To conclude, they are an essential diagnostic tool but not suited as a continuous monitoring system. The purpose of the finished product is a small device that is easy to use for everyday life, although that is outside our scope as this thesis will focus on developing the core of the device, a reliable way to scan the bladder.

Current research already exists on radar technology for scanning the bladder [5], [6]. This thesis will bring novelty to the area by using the human body as a test object, building on current research that uses phantom models, as using a human may bring new challenges regarding the construction of the radar and signal processing. This thesis also designs, manufactures, and tests a Vivaldi antenna with the PTS regulations in consideration, which is a unique feature.

2.2 Ultra-wideband (UWB)

To be considered ultra-wideband, the bandwidth shall exceed 20% of the center frequency or be at least 500 MHz compared to narrowband systems that only occupy less than 10% of the center frequency. However, narrowband systems transmit at greater power levels than UWB [9].

In Medical Application for Ultra-WideBand [7], Pan discusses the wireless technology ultra-wideband (UWB) and its potential application in medical areas, such as cardiology, obstetrics, breath pathways, and arteries. UWB pulses are generated in sub-nano second periods, making them suitable for short-distance transmission. Regarding this capability, Pan compares UWB with ultrasound as they can be applied to achieve similar goals. The main difference is that ultrasound is short-range line-of-sight technology. In contrast, UWB uses high-gain radio frequency pulses with excellent penetrating capabilities. The author also mentions some other features, such as strong multi-path resolving capability due to the exceptional signal bandwidth of UWB and low electromagnetic radiation. These properties make UWB suitable for human body imaging in hospital environments since it is non-invasive to the human body, even at short distances. It does not influence other hospital equipment as it is at a noise level [7], and the low level also

prevents sensitive information from leaking, i.e., the proposed solution presents an ethical advantage.

Distinguishing the wanted signal from background reflections and the coupling between the antennas need signal processing. Analyzing the frequency, amplitude, and phase is necessary. Furthermore, synchronizing the oscilloscope with the trigger makes it possible to stabilize the waveform, reduce noise, make repeatable measurements, and capture the signal with precise timing.

The bandwidth and pulse duration are two of the main things determining the range resolution of a pulsed radar system. A high range resolution is essential when distinguishing a target close to other, non-interesting ones, and a wider bandwidth and shorter pulse duration increase the range resolution [10]. Hence, ultra-wideband radars have the potential of a range resolution of a few centimeters or even millimeters, which is optimal when trying to detect targets in the human body. The lower end of the frequency range provides good penetration depth, and the higher end offers good resolution. The range resolution is described as [Eq. \(1\)](#):

$$S_r \geq \frac{c_0 \cdot \tau}{2} \quad (1)$$

Where c_0 is the speed of an electromagnetic wave in the material and τ is the pulse width.

2.3 Ultra-wideband as a bladder scanner

When the signal traverses through the body, a reflection will appear for each boundary between two materials of different dielectric properties. The receiving antenna catches the reflections, and the extent of the received signal depends on the difference in dielectric properties. A more significant difference results in a greater signal. Urine has a relative permittivity of $\epsilon_r = 81$ [6], and a study by Gabriel et al. [11] in 1996 showed that the relative permittivity of the bladder at around 4 GHz is $\epsilon_r \approx 20$. Hence, the ratio is approximately 1:4, and the reflection of the transmitted signal should be significant when the bladder contains urine. If the bladder is empty, no extensive reflection will appear. Surrounding tissue does not differ significantly from the bladder walls and will not give competitive signals ($\epsilon_{r, \text{skin}} \approx 38$, $\epsilon_{r, \text{fat}} \approx 5$, [11]). The ratio between fat and muscle is the same as muscle and urine, however, the reflection from fat to muscle is constant, contrary to the reflection from muscle and urine. The only reflection that will be more significant is when the signal goes from air to body since the relative permittivity in a material is in relation to air, and the relation between air and skin is approximately 1:38 for 4 GHz [11]. [Figure 1](#) shows a simple model of the body layers, color-coordinated according to their relative permittivity. The transmitted signal will reflect as the figure depicts.

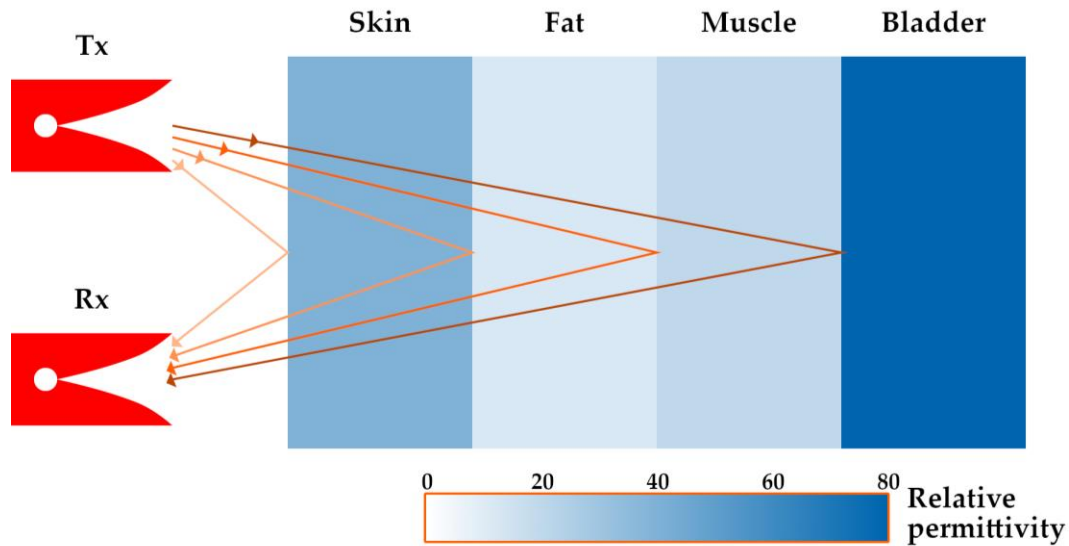


Figure 1: Simplified model of different body layers with different relative permittivity and the supposed reflections of the transmitting antennas (TX) signal being picked up by the receiving antenna RX. The image does not represent the thicknesses of the different layers.

O'Halloran et al. [5] state that the reason for using UWB is the possibility of transmitting large amounts of data with low power for a short distance with excellent resolution. Li et al. [6] stated that by combining UWB and radar technology, water accumulation in the human body is possible to detect "through the reflection from the boundary of muscle and urine" (p. 150). The signal transmits multiple body layers, and transmitted electromagnetic waves reflect for each boundary between two layers with different relative permittivity. Research shows that it is possible to distinguish urine from surrounding body tissues and organs that the signal transmits through (skin, muscle, fat) because of its significantly larger relative permittivity, ϵ_r . O'Halloran et al. [5] took advantage of the dielectric properties of both the bladders structure and urine, stating that "at microwave frequencies, an electromagnetic reflection generates at both the anterior and posterior bladder wall" (p.624) and that by extracting the information between these reflections they get the exciting parameter, urine. The study divides the state of the bladder into three stages. Each stage has a respective bladder depth (distance between the anterior and posterior bladder wall): small, medium, or full. The motivation is that it will be more resilient to between-patient variations in body tissue instead of using algorithms to approximate the bladder's exact depth. The three urine stages' depths are used as middle layers in the phantom model, with one layer of tissue-mimicking material on either side [5].

O'Halloran et al. divided the experiment into two parts with different thicknesses of the muscle tissue layers. The goal was to let an algorithm determine the phantom bladder's stage (small, medium, or full). Part one used smaller bladder depths, and the algorithm determined the bladder stage with an accuracy of 95.77%. Part two used wider bladders and achieved an accuracy of 91.63% [5]. The measured data in the study by Li et al. showed a distinction between when the target contained water

and when it was empty [6]. However, both Li et al. and O'Halloran et al. concluded that their projects only studied a phantom model and did not account for the complexity of a human bladder.

Further development would require a more realistic model, which this thesis intends to do. The intent is also to use a different frequency range and supply power per PTS regulations, and with a Vivaldi antenna exclusively designed to fit the regulations. 3D simulations will help to comprehend and test the system before physical experiments.

O'Halloran et al. [5] also proclaim the importance of recognizing non-interesting and unwanted signals such as noise and ghost targets, especially for UWB, since its signal has low transmitting energy. However, their study only examines a phantom model; noise can easily be outlined by removing it and doing measurements. Performing this procedure on a human body is impossible, which confirms the novelty and relevance of using more realistic models. Distinguishing the wanted signal from background noise is more complex: it will not be possible to measure the noise of a human body without a bladder in this thesis. However, measuring the bladder when empty gives a ground level from which the following measurements can proceed.

2.4 Phantom Model

Using a phantom model is an intermediate step in complexity between simulations and human application. Other studies utilize a multilayered structure model to achieve more realistic results [5][6]. Li et al. and O'Halloran et al. use two outer layers with similar dielectric properties to human muscle to imitate tissue and a middle layer representing the inside of the bladder. O'Halloran used a 0.5% saline solution to represent the urine, and Li et al. used seawater. The middle layer's width was altered to represent an empty bladder (smaller middle layer), respectively a full(er) bladder (wider middle layer). Li et al. used 35 mm as a full bladder and 5 mm as an empty one (without seawater), and the muscle-mimicking layers are 30 mm wide [5]. O'Halloran et al. divided their experiment into two parts: the first used a muscle depth of 10 mm, and the second used 25 mm. The depth of the phantom bladder was threefold (small, medium, or full); in part one, they were of bladder depth (10, 20, respectively 30 mm), and in part two, they were of bladder depth (20, 30, respectively 40 mm) [4]. The phantom model by Li et al. is in a case made of Styrofoam since it does not absorb the signal, while O'Halloran et al. used thin sheets of acrylic. [Figure 2](#) shows a diagram of the multilayered phantom model.



Figure 2: Diagram of a full bladder phantom model (muscle-urine-muscle).

2.5 Antenna Design

When designing a radar system, the antenna design is one of the things that determines its performance. The radar in this project requires an antenna suitable for a broad bandwidth and a stable, directional radiation pattern to penetrate the body properly. Many antennas are suitable for directional UWB applications, such as the monopole and tapered slot antennas. Although, directional monopole antennas are undesirable because of their high development costs and manufacturing complexity. Tapered slot antennas, on the other hand, have a low manufacturing cost and a more straightforward design due to their planar structure [12].

2.5.1 Tapered Slot Antennas

UWB technology widely uses tapered slot antennas (TSA), high-gain antennas that radiate in a broad spectrum. The name originates from the shape of the etched slot-line in the metallization on a dielectric substrate. There are multiple different types of TSAs, depending on how the tapered slot is formed [13], and the bandwidth of the antenna is mainly based on three parameters:

- The shape of the radiation element/taper
- The properties of the substrate it is printed on
- The feeding mechanism of the antenna

The Vivaldi antenna, introduced by Gibson in 1979 [14], has an exponential taper given by [Eq. \(2\)](#).

$$y = \pm A \cdot e^{px} \quad (2)$$

y is half of the taper width, x is the length parameter, and p is the rate at which the taper opens, determining the beamwidth. The origin is at the top of the antenna, where the waves enter free space. The slotlines separation should at least contain half the width of the longest and shortest operating wavelengths, as the part of the taper

with the same width as the current wavelength is the part of the antenna that radiates most efficiently [15].

The antenna size depends on the operating frequencies. The width should exceed half the longest operating wavelength's length, corresponding to the lowest operating frequency. In contrast, the length of the antenna should be at least one wavelength of the lowest operating frequency [15].

[Eq. \(3\)](#) gives the optimal width of the antenna, which is the effective wavelength at the lowest operating frequency, f_L .

$$W = \frac{c}{f_L} \sqrt{\frac{2}{\epsilon_r + 1}} \quad (3)$$

Where ϵ_r is the relative dielectric constant of the substrate, and c is the speed of an electromagnetic wave in vacuum. The length of the antenna should be approximately double the width.

Other designs are the linear tapered slot antenna (LTSA) and the constant antenna (CWSA) [13].

The other factor that has an impact on the bandwidth is the substrate properties. These are dielectric thickness and dielectric constants. It is preferred to use a thin substrate material with a low dielectric constant; the thickness should be less than 3% of the free space wavelength correlating to the center frequency of the desired spectrum [9]. This thesis will use an FR4 substrate with a dielectric constant of 4.3 and a thickness of 1.6 mm, which is 2.19% of the center frequency.

2.5.2 Antenna Feed

The feed of the antenna should impedance match, i.e., the characteristic impedance Z_0 , should be 50Ω . The standard way to do this is using a microstrip feed line since it is reliable, easily fabricated, and designed [16].

A popular design is called microstrip-to-slotline feeding, where the slotline is the tapered slot on the top layer of the substrate, and the microstrip is the feeding on the bottom layer. The reason is that slotline is better suited for TSAs; however, the circuit is in a microstrip transmission medium. A transition between the two is needed, and this is what is called the microstrip-to-slotline transition. The given transition is also preferred since it sustains a strictly planar design [20].

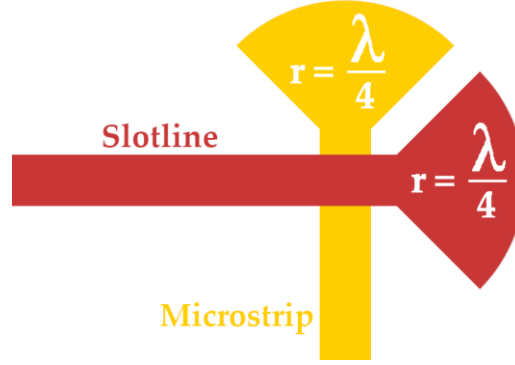


Figure 3: Microstrip-to-slotline transition with quarter-wavelength radial stubs orthogonal to each other.

The two lines are orthogonal and should surpass each other with a length of one quarter-wavelength [20], as [Figure 3](#) shows. In some designs, the lines end with radial stubs. The microstrip stub's radius and the slotline stub's diameter should be one-quarter wavelength. The slotline has a short stub and the microstrip an open stub; hence, the microstrip radial stub acts as a short circuit and the slotline stub as an open circuit at the frequency range used in this thesis. This design makes the antenna achieve a broader bandwidth since the radial stubs cancel each other's reactance.

[Eq. \(4\)](#) gives the effective dielectric constant of the slotline:

$$\varepsilon_{eff} = \frac{\varepsilon_r + 1}{2} \quad (4)$$

[Eq. \(5\)](#) gives the effective dielectric constant of the microstrip:

$$\text{If } \left(\frac{W}{H}\right) > 1: \varepsilon_{eff} = \frac{\varepsilon_r + 1}{2} + \left(\frac{\varepsilon_r - 1}{2\sqrt{1 + 12\left(\frac{H}{W}\right)}}\right) \quad (5)$$

Where H is the height of the substrate, W is the width of the microstrip, and ε_r is the relative dielectric constant of the substrate. [Eq. \(6\)](#) then gives the guide wavelength.

$$\lambda_g = \frac{\lambda_0}{\sqrt{\varepsilon_{eff}}} \quad (6)$$

2.5.3 Impedance matching

The antenna will have an SMA connector attached to the feeding mechanism, and the SMA connector has an impedance of 50Ω [20]. [Eq. \(7\)](#) gives the impedance of the microstrip, which should match the 50Ω :

$$Z_0 = \frac{87}{\sqrt{\epsilon_r + 1.41}} \ln \left(\frac{5.98 \cdot h}{0.8 \cdot w + t} \right) \quad (7)$$

Where h is the substrate thickness, w is the microstrip width, t is the trace thickness, and ϵ_r is the relative dielectric constant of the substrate.

2.6 EM simulations

There are two solvers to simulate the antenna in Advanced Design System (ADS, [15]); Momentum and FEM. Momentum uses a mixed potential integral equation that expresses the electric and magnetic fields as a combination of vectors and scalars, with the unknowns being the electric and magnetic currents. Momentum is limited for higher frequencies. [Eq. \(8\)](#) the cutoff frequency.

$$f_{cutoff} = \frac{0.4 \cdot Z_0}{h} \quad (8)$$

where Z_0 is the characteristic impedance, and h is the substrate height [22]. In our case the $f_{cutoff} = 12.5$ GHz, since $h = 1.6$ mm and $Z_0 = 50 \Omega$. The FEM simulator on the other hand uses Maxwell's differential equation. To be able to solve Maxwell's equations with traditional numerical methods, they are transformed into matrices. The problem is broken down into minor tetrahedral elements, each tetrahedron having four triangular faces. The simulator stores information about the vector field at each vertex of the tetrahedron, including the components tangential to the edges and at the midpoint of selected edges, tangential to a face, and normal to the edge. These nodal values are used to interpolate the field inside each tetrahedron. An adaptive solution method can be used additionally to increase accuracy. The initial coarse mesh is refined and restimulated multiple times depending on end boundary conditions [23].

This thesis requires using the Momentum simulator during the antenna creation as these simulations give more accurate results for planar structures such as PCB antennas. For the simulations examining the phantom models, the FEM simulator is better because of its superiority for three-dimensional environments. [24].

2.7 Radar design

Besides the antennas, the system will contain a trigger, pulse generator, and oscilloscope. The trigger helps to ensure accurate timing and synchronization of the UWB pulses; hence, it is connected to both the pulse generator and the oscilloscope. It initiates the UWB radar system to start emitting a pulse. The pulse generator produces pulses with a short duration. An antenna transmits the signal, which hits the target and reflects. The receiving antenna picks up the reflections, which are then sent to the oscilloscope to be synchronized with the trigger and processed. Hopefully, valuable data will be visible. The trigger determines the pulse repetition rate (PRR), and the pulse generator determines the pulse duration. Together they

give the duty cycle with [Eq. \(9\)](#), which should be less than 5%, to satisfy the PTS regulations.

$$Duty\ cycle = \frac{Pulse\ duration}{Total\ cycle\ time} \times 100\% \quad (9)$$

Where the total cycle time is the inverse of PRR, the time between the pulses is called receiver time and should be much slower than the pulse duration.

2.7.1 Signal processing

To locate and analyze the signal, signal processing is necessary. Especially when the signal is low in amplitude as UWB pulses are. FFT (Fast Fourier Transform) is an algorithm that computes the DFT (Discrete Fourier Transform) of a signal in a reduced amount of time, and it helps to distinguish the signal from noise. It transforms the signal to show the frequency components, which makes it easier to get wanted information [25]. Either the oscilloscope performs the transform directly or afterward in software like MatLab. Exponential smoothing then smooths the DFT of the signal to improve clarity and remove unwanted noise. This algorithm uses predictive forecasts with a smoothing constant α based on prior data. The value of α determines the dampening of the data.

In the processed data of the time domain, it should be possible to see two peaks representing the anterior and posterior bladder wall, and the thickness of the bladder can be calculated with [Eq. \(10\)](#), where Δt is the time between the peaks and c_r is the speed of light in the material.

$$d = c_r \cdot \frac{\Delta t}{2} \quad (10)$$

3 Methods

This chapter describes the methodology to answer the thesis's research questions. The first part describes the design process of the antenna operating in the chosen frequency range, the PTS-permitted range of 3.1 - 4.8 GHz.

3.1 Antenna Design

The 3.1 - 4.8 GHz frequency range results in the lowest, center, and highest operating frequencies presented in [Table 1](#).

Table 1: Frequency limits for the antenna based on the PTS regulations in the EU and the corresponding free space wavelengths.

	Frequency [GHz]	Free space wavelength [mm]
Lowest	3.10	96.71
Center	3.95	75.90
Highest	4.80	62.46

[Eq. \(2\)](#) gives taper curve:

$$y = \pm A \cdot e^{px}$$

The width of the antenna from [Eq. \(3\)](#):

$$W = \frac{c}{f_L} \sqrt{\frac{2}{\epsilon_r + 1}} = \frac{3E8}{3.1E9} \sqrt{\frac{2}{4.3 + 1}} = 59.44 \text{ [mm]}$$

It results in a length of $L = 118.89$ mm since it should be double the width.

[Eq. \(4\)](#) gives the effective dielectric constant of the slotline and [Eq. \(6\)](#) gives the guide wavelength for the slotline:

$$\epsilon_{eff} = \frac{\epsilon_r + 1}{2} = \frac{4.3 + 1}{2} = 2.65$$

$$\lambda_{g,slotline} = \frac{\lambda_0}{\sqrt{\epsilon_{eff}}} = \frac{0.0759}{\sqrt{2.65}} = 0.0466 \text{ [m]}$$

[Eq. \(5\)](#) gives the effective dielectric constant of the microstrip, and [Eq. \(6\)](#) gives the resulting guide wavelength for the microstrip, with the height of the substrate $H = 1.6$ mm, the width of the microstrip $W = 1$ mm, and the relative dielectric constant $\epsilon_r = 4.3$:

$$\text{If } \left(\frac{W}{H}\right) > 1: \varepsilon_{eff} = \frac{\varepsilon_r + 1}{2} + \left(\frac{\varepsilon_r - 1}{2\sqrt{1 + 12\left(\frac{H}{W}\right)}}\right) = \frac{4.3 + 1}{2} + \left(\frac{4.3 - 1}{2\sqrt{1 + 12\left(\frac{0.0016}{0.001}\right)}}\right) = 3.017$$

$$\lambda_{g,microstrip} = \frac{\lambda_0}{\sqrt{\varepsilon_{eff}}} = \frac{0.07312}{\sqrt{3.017}} = 0.0437 \text{ [m]}$$

Which results in the radial stub of the slotline having a diameter of $d = \lambda_{g,slotline}/4 = 11.65$ mm, and the radial stub of the microstrip to have a radius of $r = \lambda_{g,microstrip}/4 = 10.92$ mm.

3.1.1 Impedance matching

The width of the microstrip is $w = 1$ mm, the trace thickness of the printer is $t = 0.0035$ mm, the substrate thickness is $h = 1.6$ mm, and according to [Eq. \(7\)](#) the microstrip line impedance is:

$$Z_L = \frac{87}{\sqrt{\varepsilon_r + 1.41}} \ln\left(\frac{5.98 \cdot h}{0.8 \cdot w + t}\right) = \frac{87}{\sqrt{4.3 + 1.41}} \ln\left(\frac{5.98 \cdot 0.0016}{0.8 \cdot 0.001 + 0.000035}\right) = 88.8 \text{ } [\Omega]$$

To match the $50 \text{ } \Omega$ SMA connector, the feeding line must have a tapered shape ([Figure 4](#)) where the end towards the microstrip line has a width of $w = 1$ mm, to match the microstrip line. The other end should have a width to match the $50 \text{ } \Omega$ SMA connector, which according to [Eq. \(7\)](#) equals a width of 2.98 mm:

$$Z_0 = \frac{87}{\sqrt{\varepsilon_r + 1.41}} \ln\left(\frac{5.98 \cdot h}{0.8 \cdot w + t}\right) \rightarrow w = \frac{5.98 \cdot h}{0.8e^{\frac{Z_0\sqrt{\varepsilon_r+1.41}}{87}}} - \frac{t}{0.8}$$

$$w = \frac{5.98 \cdot 0.0016}{0.8e^{\frac{50\sqrt{4.3+1.41}}{87}}} - \frac{0.000035}{0.8} = 0.00298 \text{ [m]}$$

The impedance at 3.95 GHz is $49.4 - j4.409 \text{ } \Omega$, and it can improve by iterating the microstrip lengths.

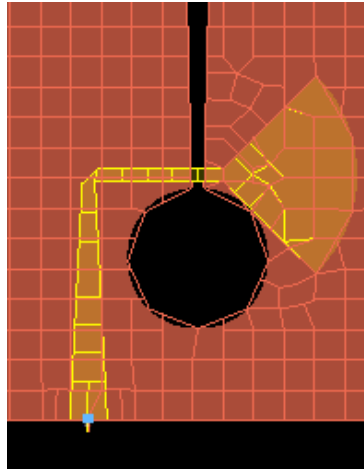


Figure 4: The designed antennas tapered-shaped feeding line.

3.1.2 Construction in ADS

The antenna is constructed in ADS according to the design theory and parameters presented in [2.5 Antenna Design](#) and calculated in [3.1 Antenna Design](#). [Figure 5](#) shows the resulting design with the parameters given in [Table 2](#).

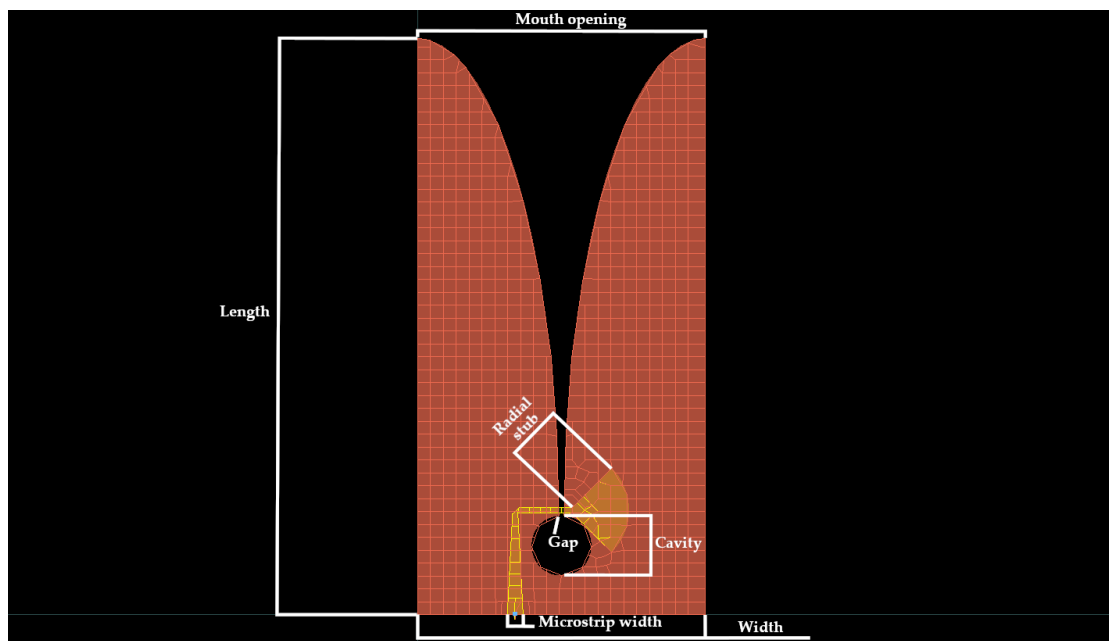


Figure 5: Antenna layout in ADS strictly designed according to theory.

Table 2: Antenna parameters before iteration.

Parameters	Measure [mm]
Width	59.44
Length	118.89
Offset	-
Mouth opening	54.2
Slotline gap	1

Cavity diameter	11.65
Radial stub radius	10.92
Microstrip width	2.98
Tapered slot equation	$y = \pm 0.5e^{0.04424x}$

The design does not have the center frequency at 3.95 GHz; instead, it has it at the frequency $f = 3.75$ GHz. The $S(1,1)$ parameter represents the reflection coefficient of the antenna and describes how much power the antenna reflects.

ADS simulations introduce many external factors which the theoretical equations do not consider. The 3D electromagnetic simulation tool in ADS called Momentum solves full-wave 3D electromagnetic equations for complex structures accounting for other factors such as parasitic effects and material properties other than dielectric constant and loss tangent. The theoretical design of the antenna has good directivity, but the VSWR is not under 2 for part of the spectrum. However, iterations on specific parameters can improve the antenna.

The iterations aim to achieve wider impedance matching. The iterative process alters the length of the L-shaped microstrip line. It introduces an offset to the sides of the antenna and increases the size of the mouth opening, as shown in [Figure 6](#), resulting in a wider antenna. By changing the size of the mouth opening, the antenna will also have a new taper rate.

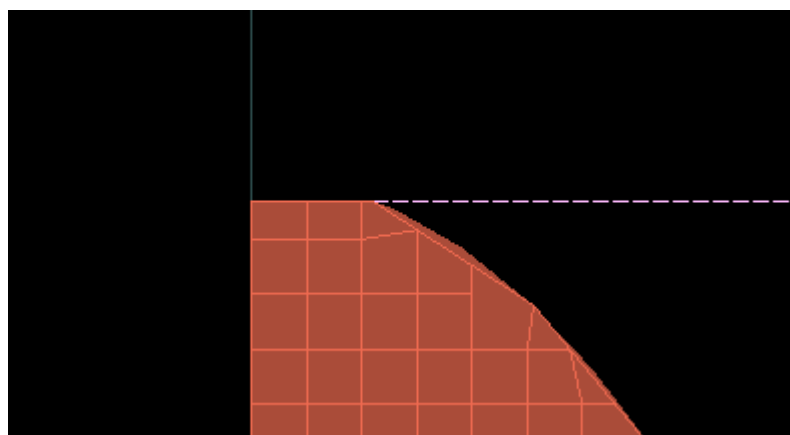


Figure 6: The added offset of 5.35 mm on the edge of the antenna's tapered slot to increase performance.

3.2 Fabrication of the antenna

The fabrication of the antenna starts with milling it on an FR4 substrate with a dielectric constant of 4.3 and a thickness of 1.6 mm using the milling machine ProtoMat S63 using the Gerber files exported from ADS. The trace width is 35 μm . After milling, the next step is attaching a 50 Ω SMA connector with a maximum frequency of 18 GHz [26] and soldering the center contact to the microstrip feed. The antennas are then attached to 3D-printed boxes with one-quarter-inch holes that fit a

camera tripod. A plate is also 3D-printed in which the boxes fit and are horizontally moveable, which helps to determine the optimal distance between the antennas. [Figure 7](#) shows the setup with the antennas attached to the boxes and to the plate that enables horizontal movement. The plate and the boxes ensure that the measurements are repeatable.

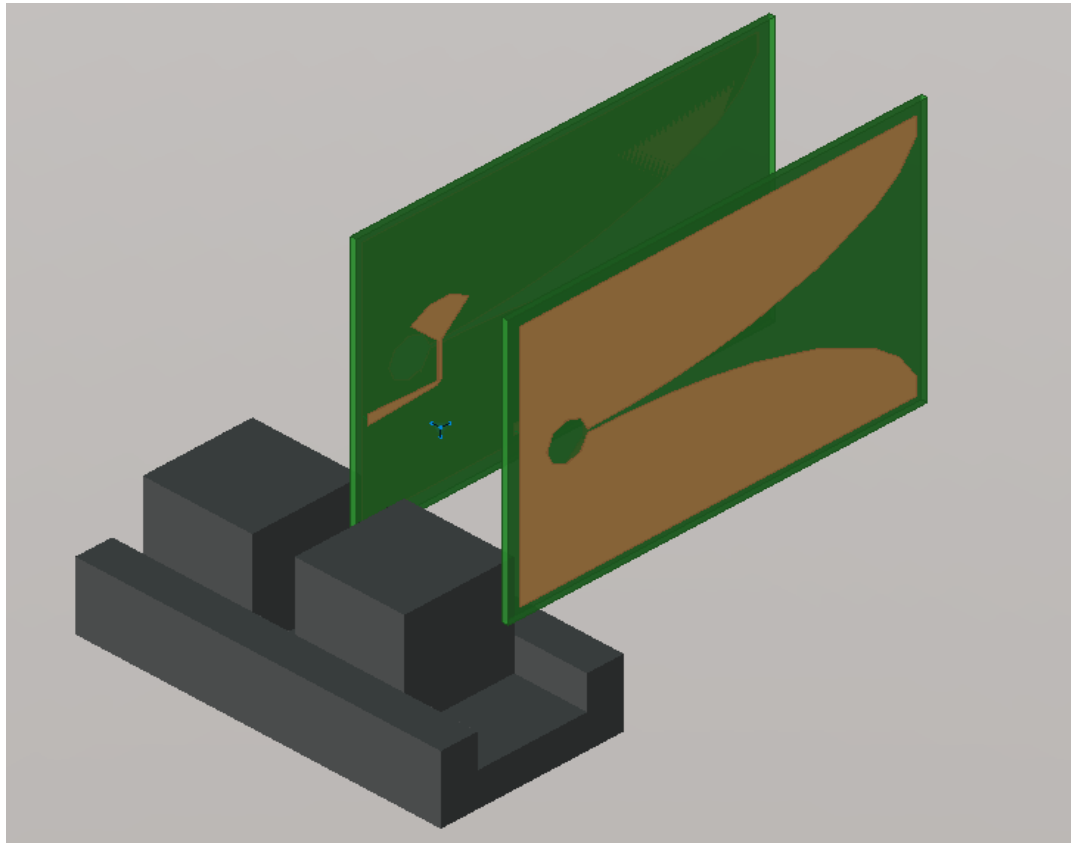


Figure 7: The antennas with the attached boxes fitted on the plate that enables horizontal movement.

3.3 Antenna characterization

Before testing the antenna in the EMC chamber and with the other radar equipment, they must be characterized and tested. Firstly, the antennas are measured with a network analyzer (E8364B PNA Network Analyzer, 10 MHz – 50 GHz), and the S-parameters are compared to the simulations ([Figure 21](#)). $S(1,1)$ for both antennas are close to the simulated values and identical to each other, indicating a stable design. [Figure 8](#) displays $S(1,1)$ for the transmitting antenna, showing that it is below -10 dB (which equates to a VSWR of 2) for the frequency range of 3.95-4.8 GHz.

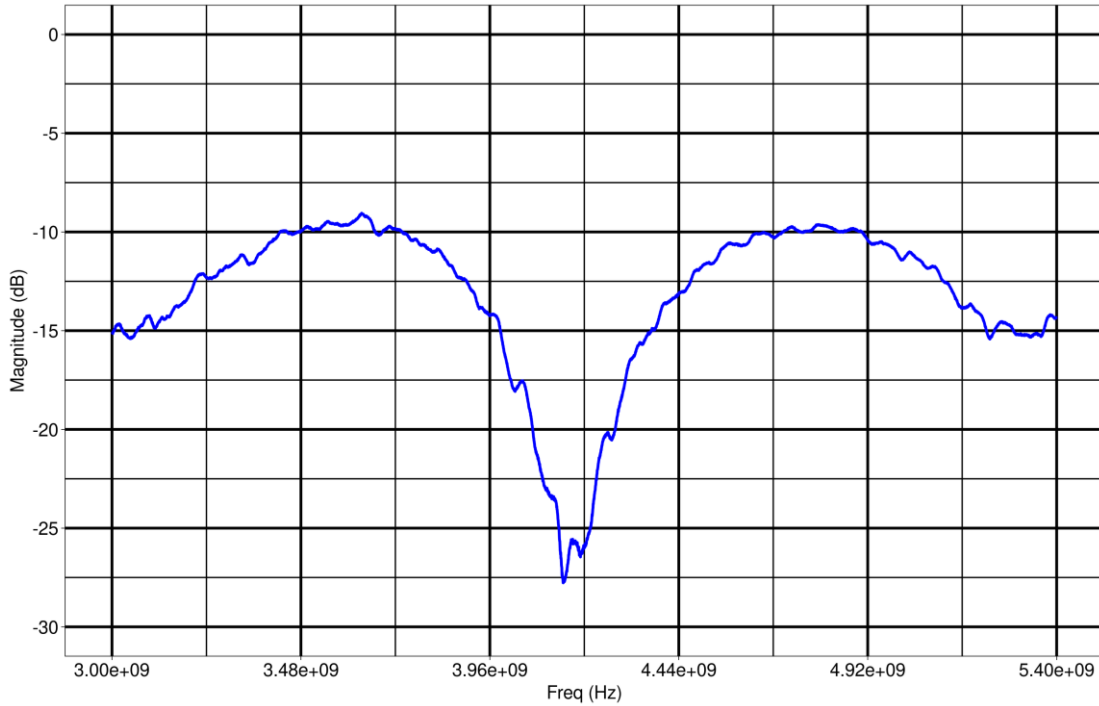


Figure 8: Measured $S(1,1)$ parameter for the transmitting antenna using a network analyzer.

The next step is to outline and compare the radiation pattern to the simulations. The transmitting antenna is connected to a signal generator (APSIN6010 9 kHz – 6100 MHz RF Signal Generator) that generates a signal at 3.95 GHz with a power of 0 dBm. The receiving antenna is connected to a spectrum analyzer (E4407B ESA-E Spectrum Analyzer, 9 kHz – 26.5 GHz). The antennas are separated by 3 m as 3 m is the separation between the antennas in the anechoic chamber where measurements will later take place, making it more comparable. Their lower edges are located 1.55 m above the floor, and the transmitting antenna is mounted on a non-reflective pillar with a horizontally turning top. The height and distances should be several wavelengths long to get minimal reflections from the surroundings. Measurements are noted every 5° . Both antennas are connected with RG316 cables. The simulated received power, P_r , is calculated from the simulated gain (G_t , G_r) for every 15° , range $r = 3$ m, wavelength $\lambda = 75.8968$ m and with the transmit power $P_t = 0.001$ W, according to Friis formula (Eq. (11)).

$$P_r = G_t G_r P_t \left(\frac{\lambda}{4\pi r} \right)^2 \quad (11)$$

The result is shown in Figure 9. When the transmitting antenna points towards the receiving antenna, the received power is the highest, indicating directional radiation. The graph shows some increase in received power where the transmitting antenna points towards reflective materials, which increases the power in the receiving antenna, even though the transmitting antenna is not pointing towards it.

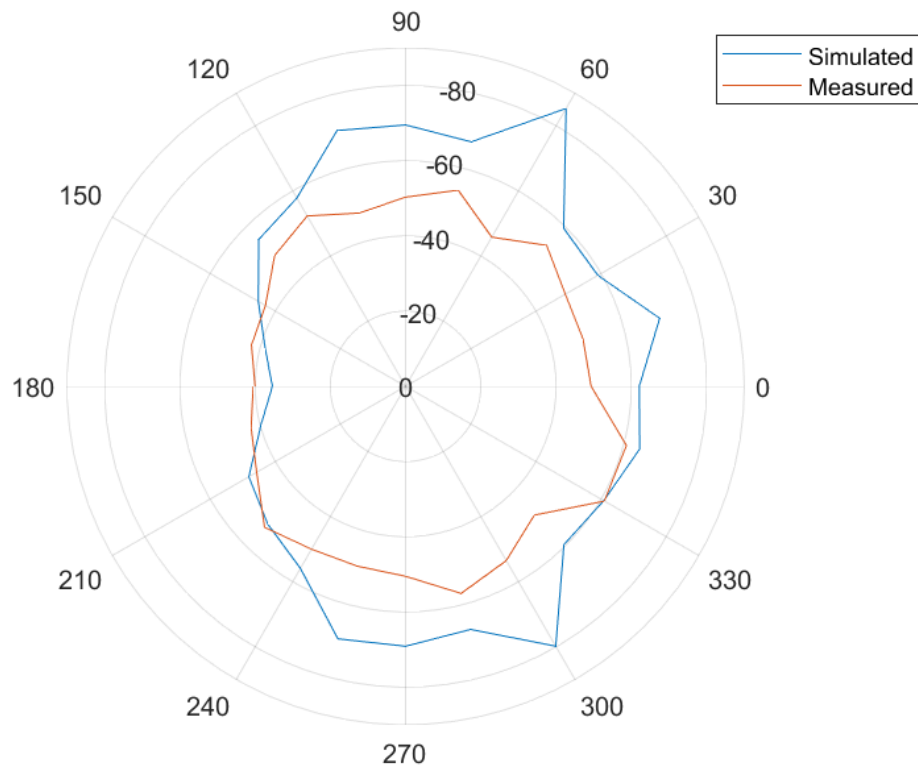


Figure 9: Measured and simulated received power in dBm every 5° when the antennas are separated with 3 m and a transmitted signal of 3.95 GHz with a transmit power of 0.001 W.

In the anechoic chamber, the Vivaldi antenna is fed with a signal of frequencies 3.1, 3.525, 3.95, 4.375, and 4.8 GHz. The chamber is set up according to the EMC specifications for the specific frequencies to get minimal reflections. An HF907 horn antenna receives the transmitted signal from the Vivaldi antenna, and measurements are taken every 5° as it turns. [Figure 10](#) shows the setup in the chamber with the absorbers surrounding the antenna mounted on a non-reflective pillar.

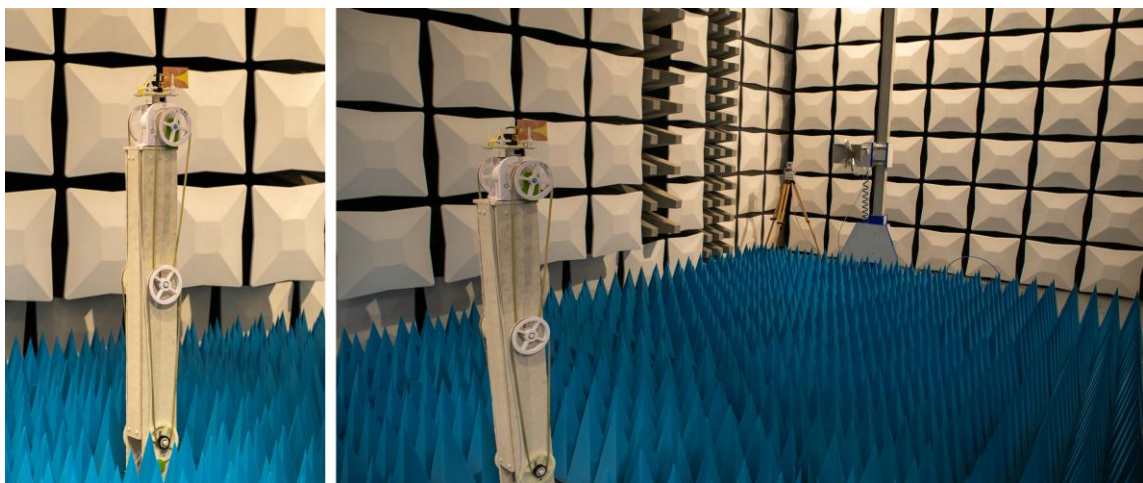


Figure 10: Setup in the anechoic chamber when measuring the antennas radiation.

3.4 Simulations in EMPro

After designing the antenna in ADS, the layout is exported to EMPro, where they are again characterized to establish their performance. The characteristics of the pulse used in the real-life setup, which is measured from the pulse generator to the oscilloscope, are imported to EMPro and are used in the simulations to make it as close to reality as possible. The phantom models that are used in the experiments are also imported to EMPro for simulations comparable to real-life experiments. [Figure 11](#) shows the setup with the antennas and the full phantom model.

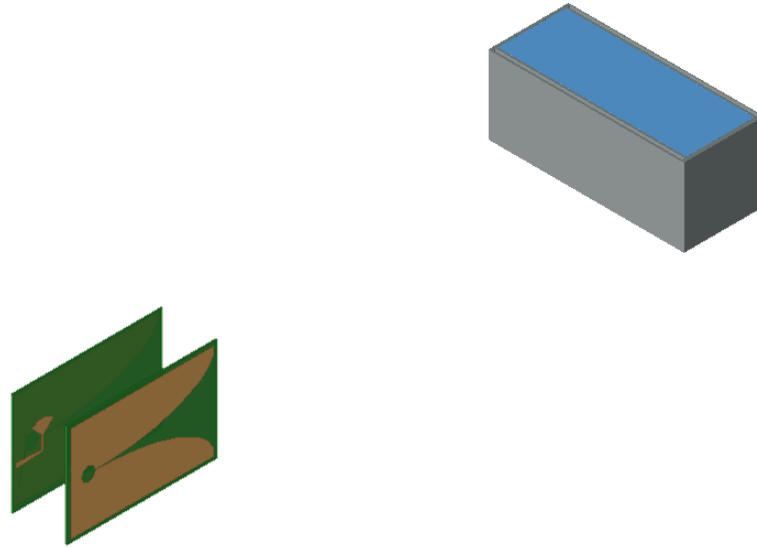


Figure 11: The setup in EMPro with the antennas imported from ADS and the full phantom model in the same design as the 3D-printed one used in the experiments.

Two simplified human torsos are also created, one with a full bladder and one with an empty bladder ([Figure 12](#)). One layer of muscle and one of fat surrounds the bladder, and the outmost layer is skin. The temperature of each material is set to 37 °C.

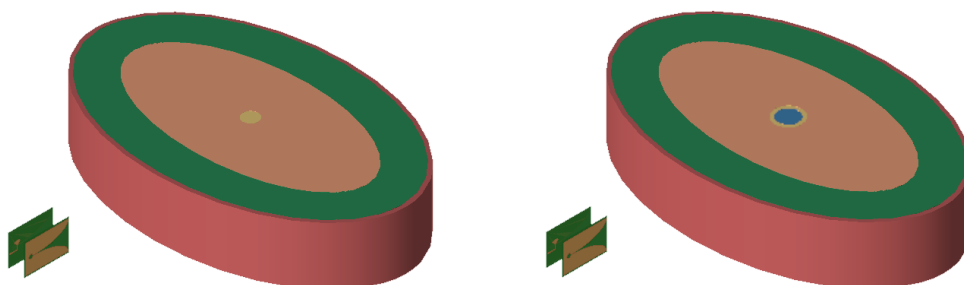


Figure 12: Simulation setup with a transmitting and a receiving antenna imported from ADS, and a simplified model of the human torso with a full bladder to the right and an empty bladder to the left. The red part is skin and has a thickness of 10 mm, the green part is fat and

has a thickness of 90 mm, the orange part is muscle with a thickness of 150 mm, and the yellow part is the bladder walls. The full bladder contains urine (in blue), and it has a radius of 4 cm. The empty bladder is smaller and does not contain urine.

Simulations are performed with a gaussian first-order derivative pulse with a pulse width of 0.25 ns (Figure 13) and with the same pulse as the one used in real-life experiments (a square pulse with a pulse width of 10 ns). One antenna transmits the pulse, and the other receives the reflections. According to Eq. (1), for a 0.25 ns pulse, the range resolution is:

$$S_r \geq \frac{c_0 \cdot \tau}{2} = \frac{3 \cdot 10^8 \cdot 0.25 \cdot 10^{-9}}{2} = 0.0375 \text{ [m]}$$

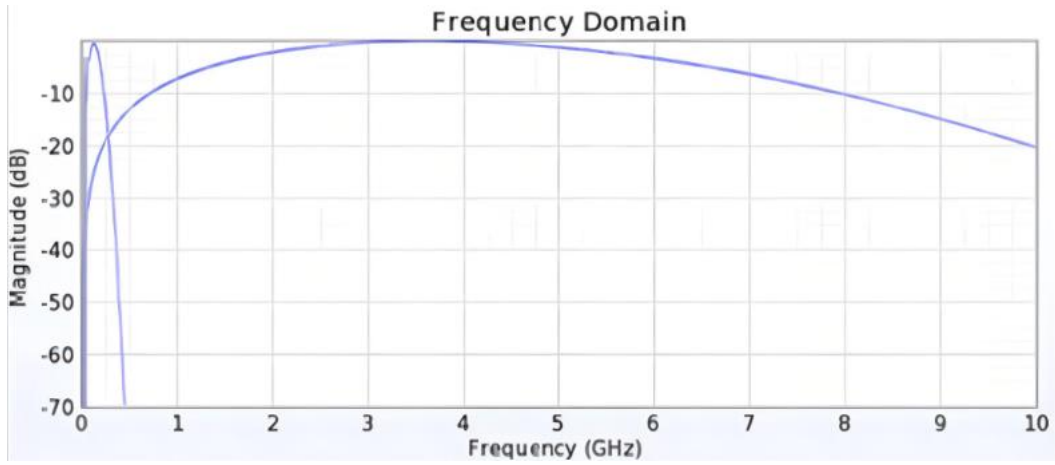


Figure 13: The upper diagram shows the frequency response of the gaussian first order derivative with pulse width 0.25 ns, and the bottom one has a pulse width of 10 ns.

3.4.1 EMPro simulation specifications

To achieve adaptive convergence, the simulator refines the mesh for each point in multiple passes to discretize the domain for numerical analysis. The delta error is set to 0.02 per pass, as lower values did not provide significant differences while considerably increasing simulation time, while the maximum number of passes is set to 20 as per the recommendation of EMPro. The target mesh size is set to be one-third of the free space wavelength at the maximum frequency while enabling edge meshing and vertex meshing. Edge meshing makes the mesh size along the edges smaller, while vertex meshing reduces the size along vertices. These are especially important as the edges and vertices are critically important points in the geometry and decreasing the mesh size along these parts can reveal finer-scale features that can change the antenna's characteristics in the simulations significantly. Other areas with simpler geometry will remain larger as they are less significant to the simulation results.

3.5 Radar design

The pulse generator (E8267D PSG Vector Signal Generator) is the only one that could be provided in time for this thesis. It is not optimal for this application, for example, the resulting range resolution is too big. It produces a pulse with a pulse width of 10 ns to the transmitting antenna via an RG316 cable and a 50 Ω RF adapter (BNC plug to SMA jack). According to [Eq. \(1\)](#) the pulse width results in a range resolution of:

$$S_r \geq \frac{c_0 \cdot \tau}{2} = \frac{3 \cdot 10^8 \cdot 10 \cdot 10^{-9}}{2} = 1.5 \text{ [m]}$$

The pulse generator produces an FWHM (Full Width at Half Maximum) square pulse [27], meaning that the pulse width is between half the amplitude on the rising edge and half the amplitude on the falling edge. [Figure 14](#) shows the pulse waveform when the pulse generator is connected directly to the oscilloscope via an RG316 cable.

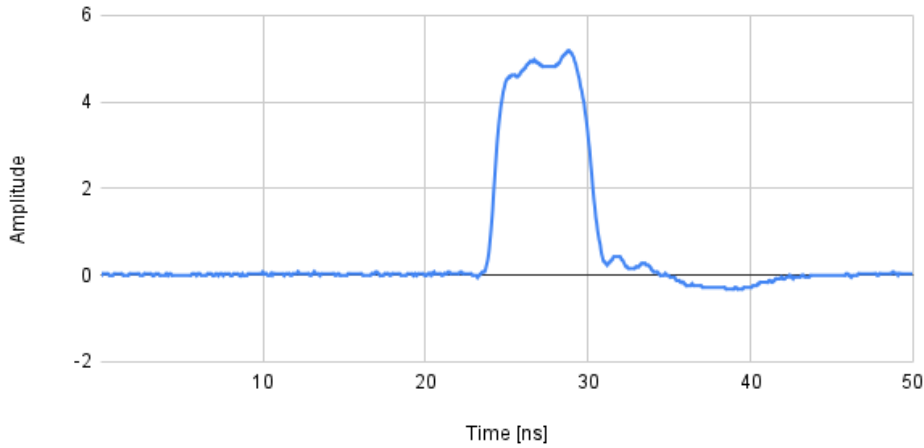


Figure 14: Waveform of the generated pulse with a pulse width of 10 ns.

The trigger is integrated in the pulse generator and the PRR is set to 1 kHz, which according to [Eq. \(9\)](#) gives a duty cycle of:

$$\text{Duty cycle} = \frac{\text{Pulse duration}}{\text{Total cycle time}} \times 100\% = \frac{10 \cdot 10^{-9}}{0.0001} \times 100\% = 0.01 \%$$

Which is below the PTS limit of 5%.

The trigger output is connected to channel 2 of the oscilloscope, while the receiving antenna is connected to channel 1 via an RG316 cable and an adapter. The trigger function in the oscilloscope synchronizes channel 1 to channel 2. The oscilloscope used is a Rohde & Schwarz RT06 with a sampling rate of 20 GSa/s and a bandwidth of 6 GHz. The oscilloscope performs a fast Fourier transform (FFT) on the received

signal, making the frequency and time domain spectrum visible. The radar system is depicted in [Figure 15](#).

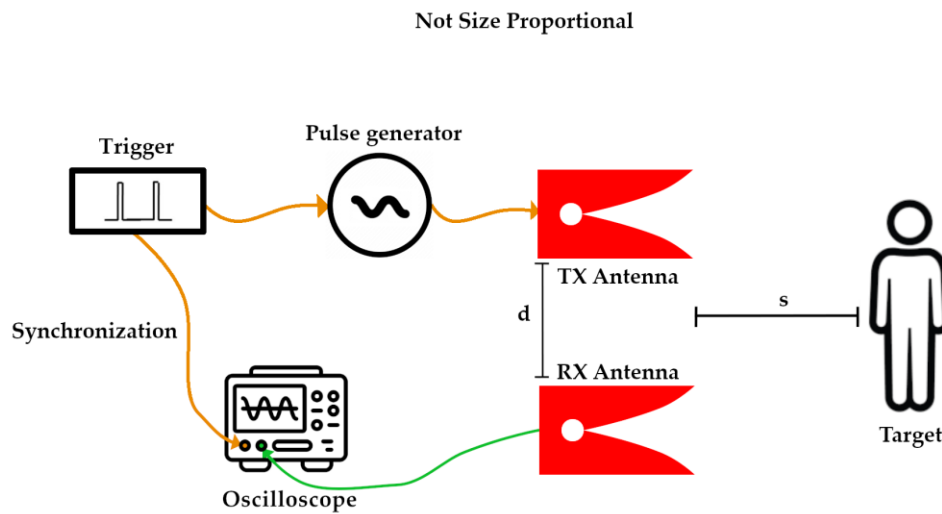


Figure 15: Layout of the radar system with a trigger, pulse generator, oscilloscope, two antennas, and the target.

3.5.1 Phantom model

Two phantom models are designed; one that represents a full bladder ([Figure 16](#)) and one that represents an empty bladder ([Figure 17](#)). The empty one is smaller (100x20x50 mm) and will only contain fluid with lower dielectric properties. The full bladder is bigger as the human bladder expands when urine flows into it. The dimensions are 150x60x60 mm, with three pockets representing the anterior bladder wall, urine, and posterior bladder wall. The bladder walls have a width of 2 mm, and the urine pocket has a width of 52 mm. 1 mm thick walls separate the pockets. The urine pocket, therefore, has a volume of 450 ml (total capacity is around 500 ml). The fluid with lower dielectric properties is mixed using water, salt, and sucrose.

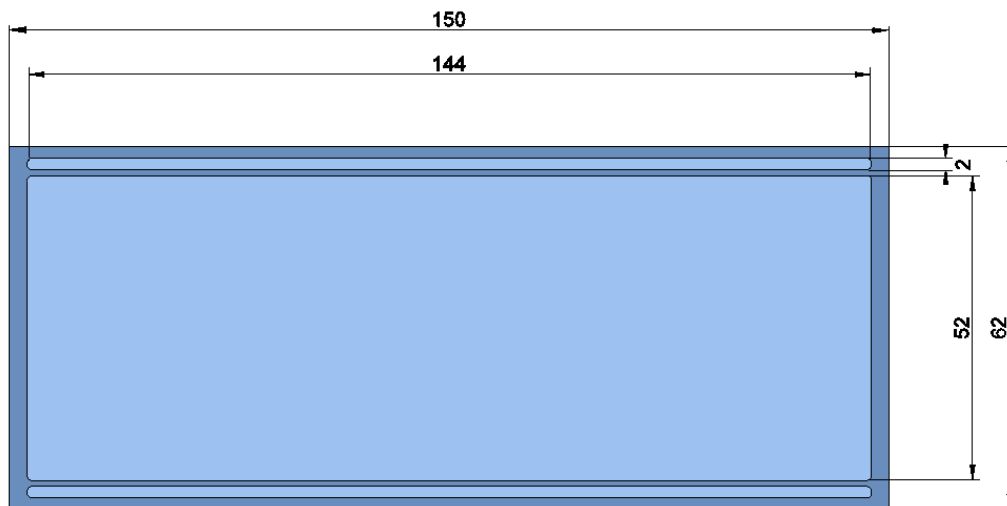


Figure 16: Layout of the phantom model of a full bladder.

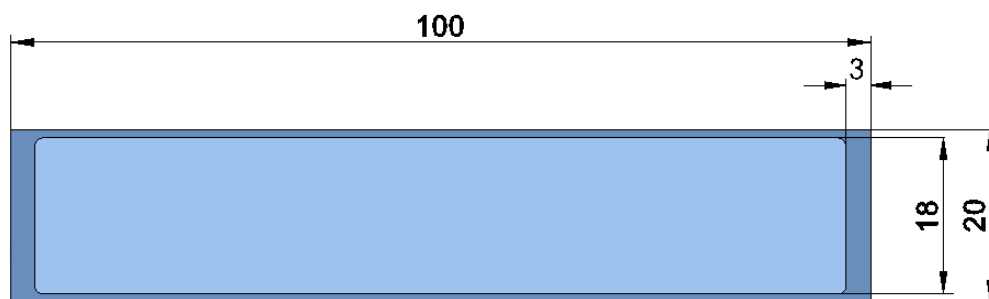


Figure 17: Layout of the phantom model of an empty bladder.

3.6 Experiments

Firstly, the experiments are performed in a busy environment and later in an anechoic chamber ([Figure 18](#)). The measurements from the receiving antenna are as follows: no transmission from the transmitting antenna, transmission with no target, phantom model with and without water, and human body pre- and post-voiding. The minimum distance between the antennas' front edges and the target is where the far-field region begins, which is three lambdas of the lowest operating frequency:

$$3\lambda_{min} = 3 \cdot 96.71 = 290.13 \text{ [mm]}$$

According to Friis formula ([Eq. \(11\)](#)), a minimum distance is optimal for the highest receiving power.

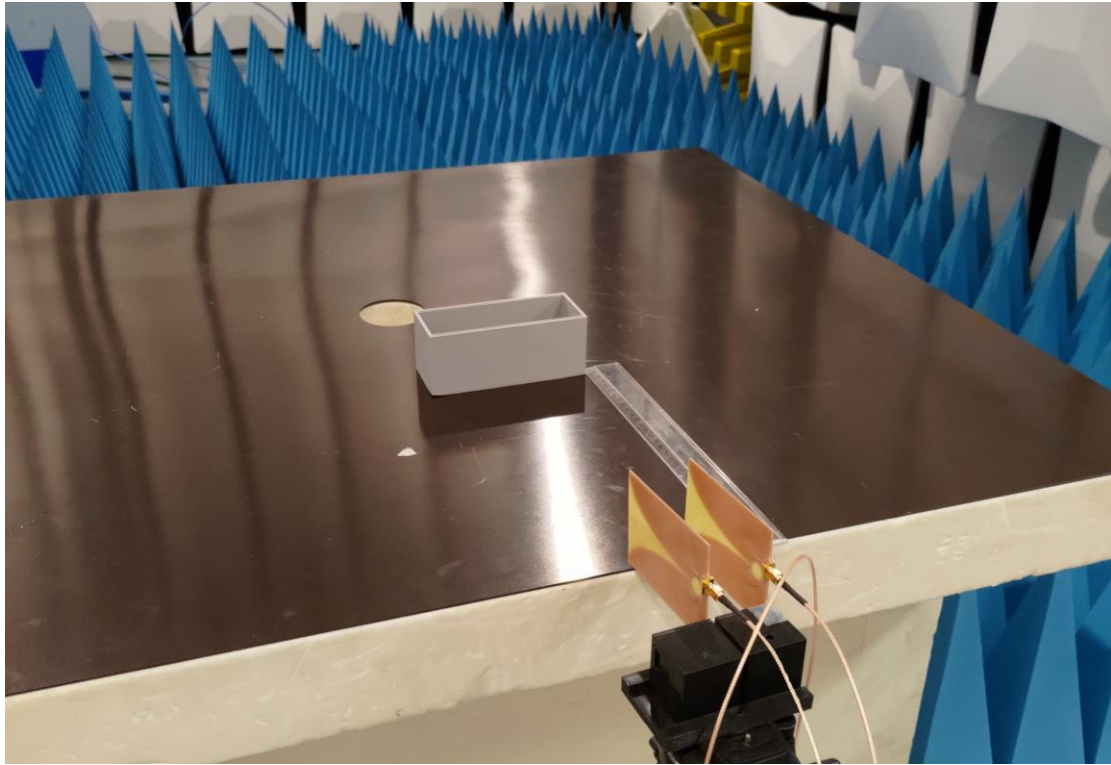


Figure 18: Setup for measurements in the anechoic chamber with a phantom model 30 cm from the antennas.

4 Results

4.1 Antenna design

Iterating the adjustable antenna parameters results in the final design shown in [Figure 19](#) with the parameters listed in [Table 3](#).

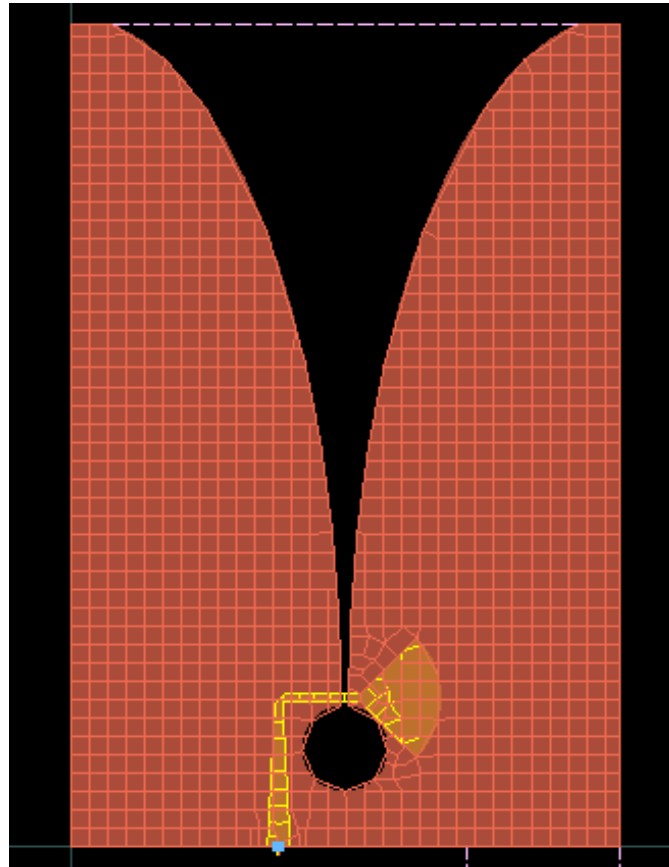


Figure 19: Layout of the final antenna design constructed in ADS.

Table 3: Antenna parameters after iterations and the initial parameters, altered values are in red.

Parameter	Final measure [mm]	Initial measure [mm]
Width	72.2	59.44
Length	108.4	118.89
Offset	5.35	-
Mouth opening	61.5	54.2
Slotline gap	1	1
Cavity diameter	11.23	11.65
Radial stub radius	10.53	10.92
Microstrip width	2.98	2.98
Tapered slot equation	$y = \pm 0.5e^{0.03804x}$	$y = \pm 0.5e^{0.04424x}$

[Figure 20](#) shows the finalized and fabricated antennas mounted on the 3D-printed boxes that can attach to a camera tripod.

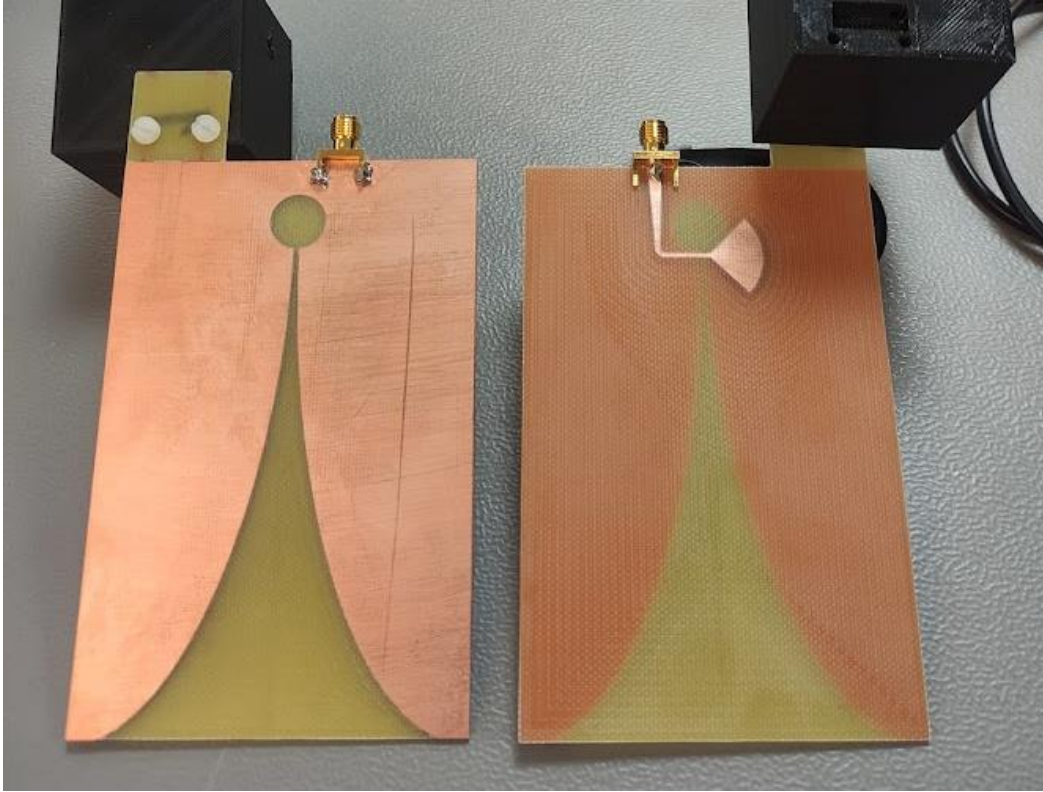


Figure 20: The top layer of the antenna is to the left, and the bottom layer is to the right.

[Figure 21](#) shows the S-parameters of the initial and final design.

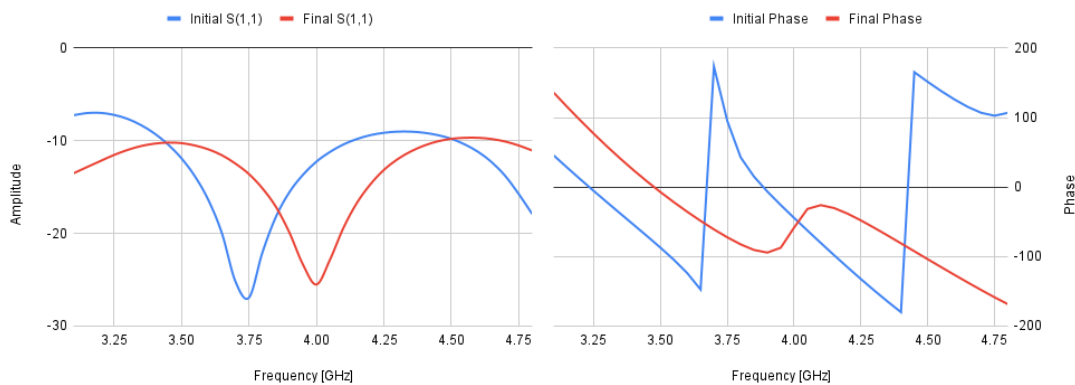


Figure 21: The S11 parameters of the antenna before and after iteration for the frequency range 3.1 - 4.8 GHz with a marker at the reflection coefficient minimum and the corresponding phase.

[Figure 22](#) shows the far-field radiation pattern for the final antenna design in the simulations and [Figure 23](#) shows the measured radiation pattern in the anechoic chamber described in [3.3 Antenna characterization](#).

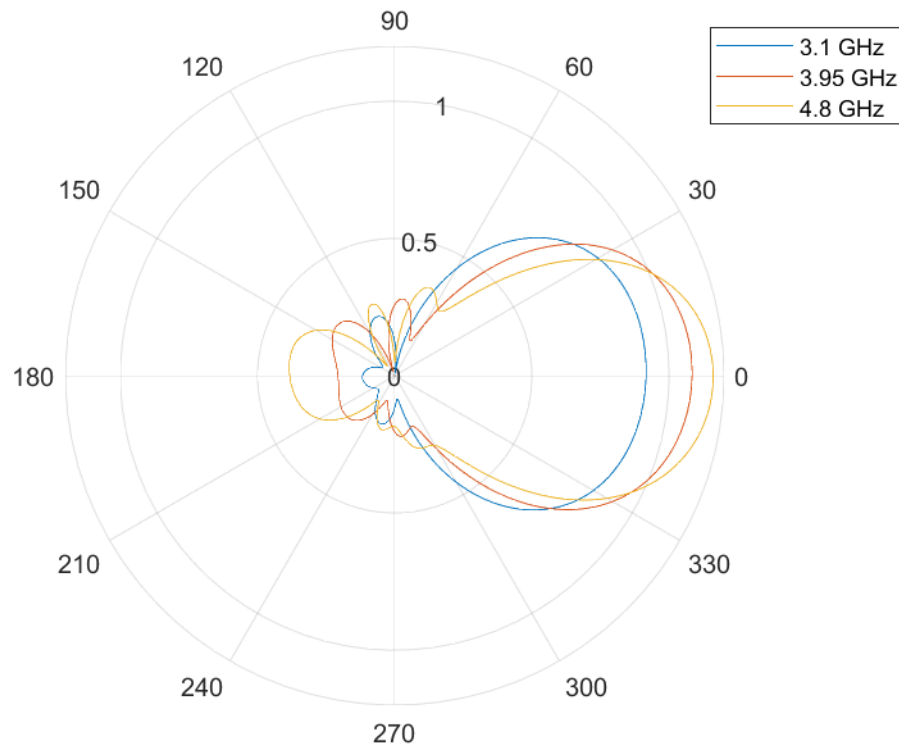


Figure 22: Radiation pattern at 3.1 GHz, 3.95 GHz, and 4.8 GHz after iterations.

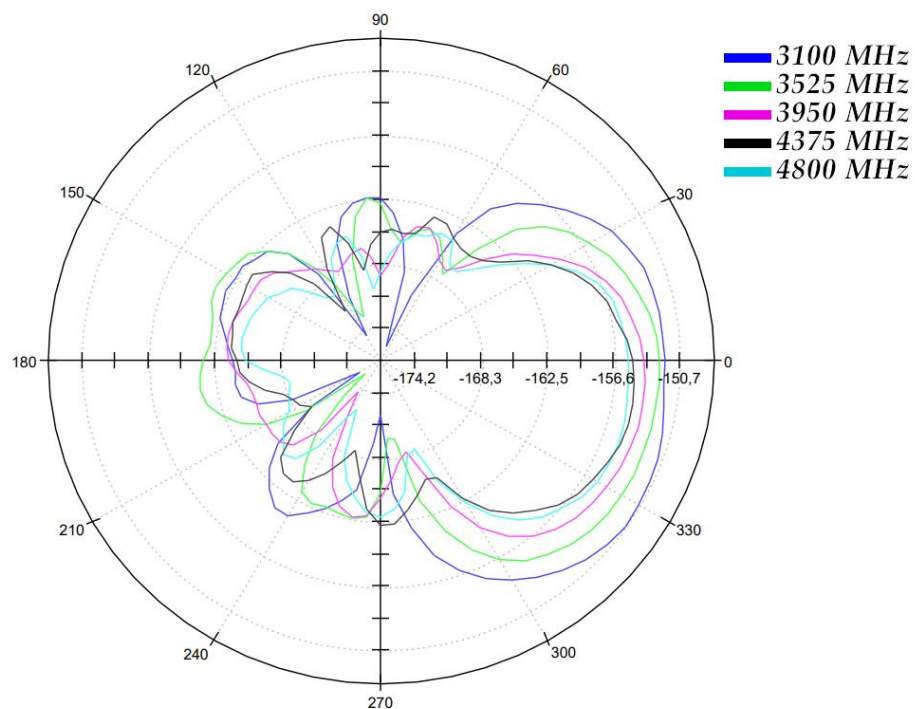


Figure 23: The Vivaldi antennas radiation pattern measured in an anechoic chamber.

The iterated antenna is more directional than the initial one. The radiation pattern has high gain with consistent coverage in the y-direction. Good coverage in the desired direction is essential to detect targets dependably, as antennas with

inconsistent coverage can easily miss them. [Figure 24](#) shows the VSWR for the initial and final antenna, which is below 2 for the entire range after iterations.

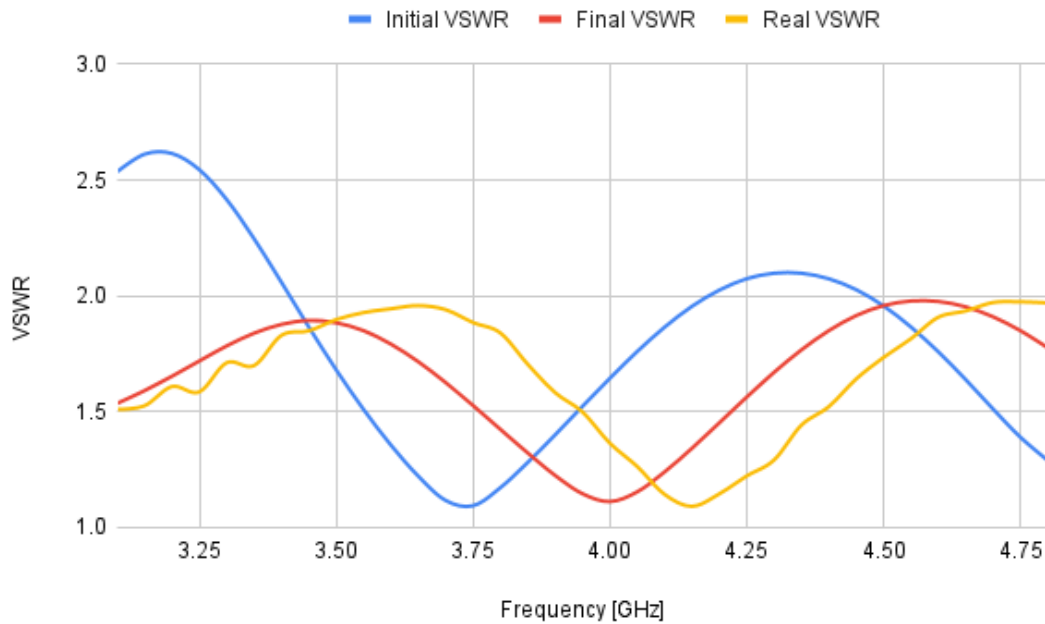


Figure 24: VSWR of the fabricated antenna measured with a network analyzer compared to the VSWR of the final and initial antenna designs in ADS for the frequency range 3.1-4.8 GHz.

[Figure 25](#) shows the impedance at the center frequency for the final antenna. After iterations on the microstrip line, the impedance matching improves to $52.65 - j4.75 \Omega$, which is closer to 50Ω compared to the initial impedance of $46.4 - j2.55 \Omega$.

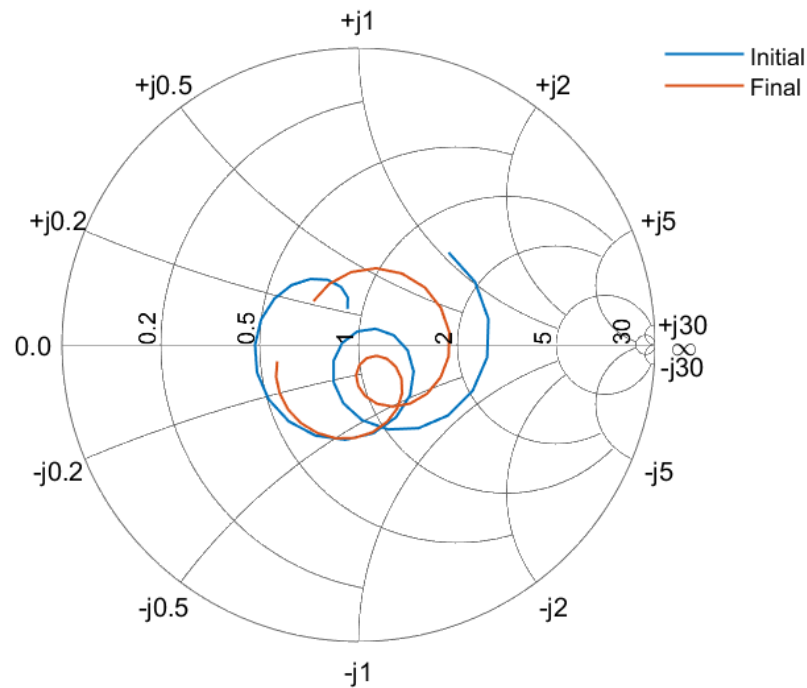


Figure 25: Smith chart representation of the reflection coefficient. The impedance for the final design is $Z = 52.65 - j4.75 \Omega$ at 4 GHz.

Figure 26 shows the schematic of the microstrip feed after alterations on the taper length and microstrip line. MTaper is the impedance matching element, MRStub is the stub of one-quarter wavelength, and MBend and MLIN are iterated along with the length of MTaper. MRStub contains the substrate parameters. Zin shows where the port is along with Term1, which has an impedance of 50 Ω .

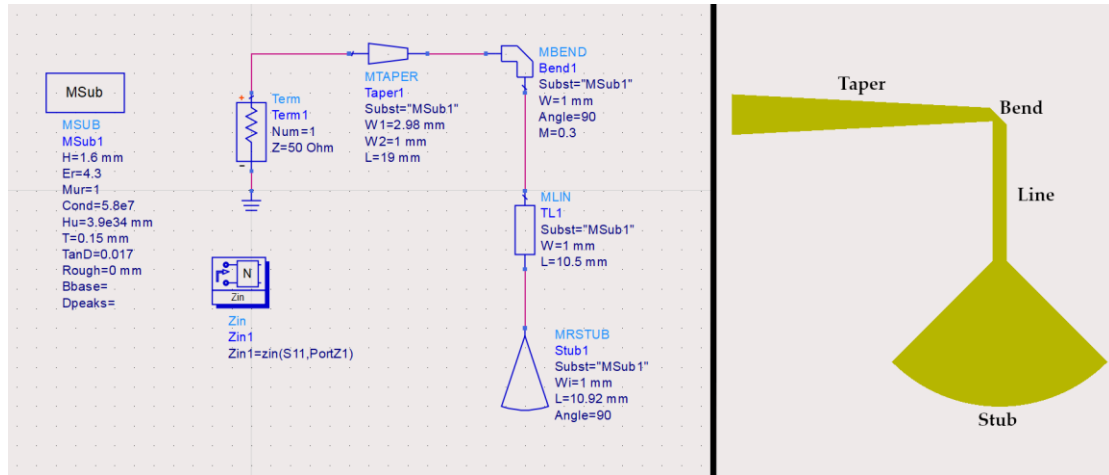


Figure 26: Equivalent circuit of microstrip feed after alterations and the corresponding microstrip geometries.

4.2 Radar

Figure 27 shows the processed data of the different measurements (empty and full phantom model and no transmission) with a dampening of $\alpha = 0.99$.



Figure 27: The received signal from measurements with empty and full phantom models, and no transmission. The data has exponential smoothing with $\alpha = 0.99$.

Figure 28 shows the measured results with a logarithmic scale on the x-axis and with the measured frequency components of the pulse.

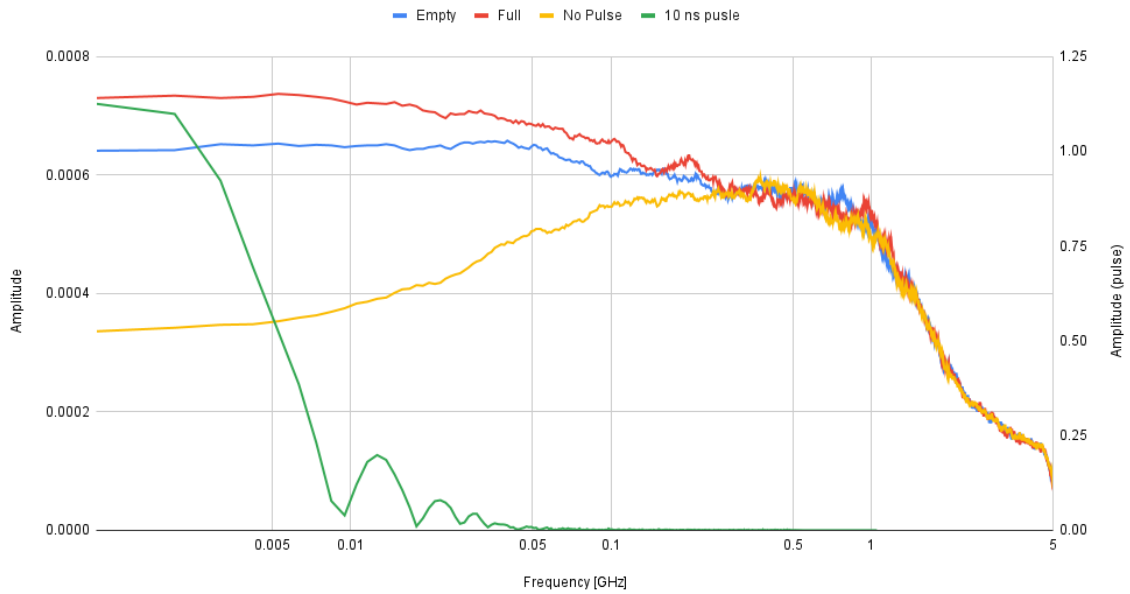


Figure 28: Received signal (after FFT and exponential smoothing) compared to the 10 ns pulse frequency response measured with the oscilloscope directly from the pulse generator.

[Figure 29](#) shows the measured results when altering the distance between the transmitting and the receiving antennas, to see how they affect each other. The minimal distance is 4 cm due to the cubes attached to the antennas.

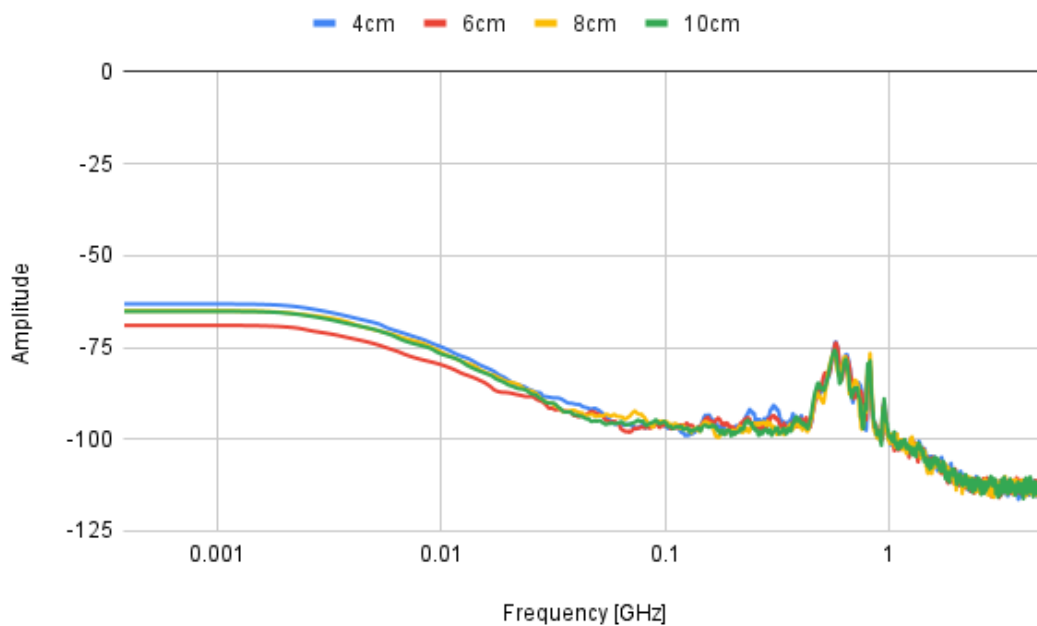


Figure 29: The measured results from altering the distance between the transmitting and receiving antennas with distances 4, 6, 8, and 10 cm.

[Figure 30](#) shows the experiments performed on a human body pre- and post-voiding. The body is positioned 30 cm from the antennas.

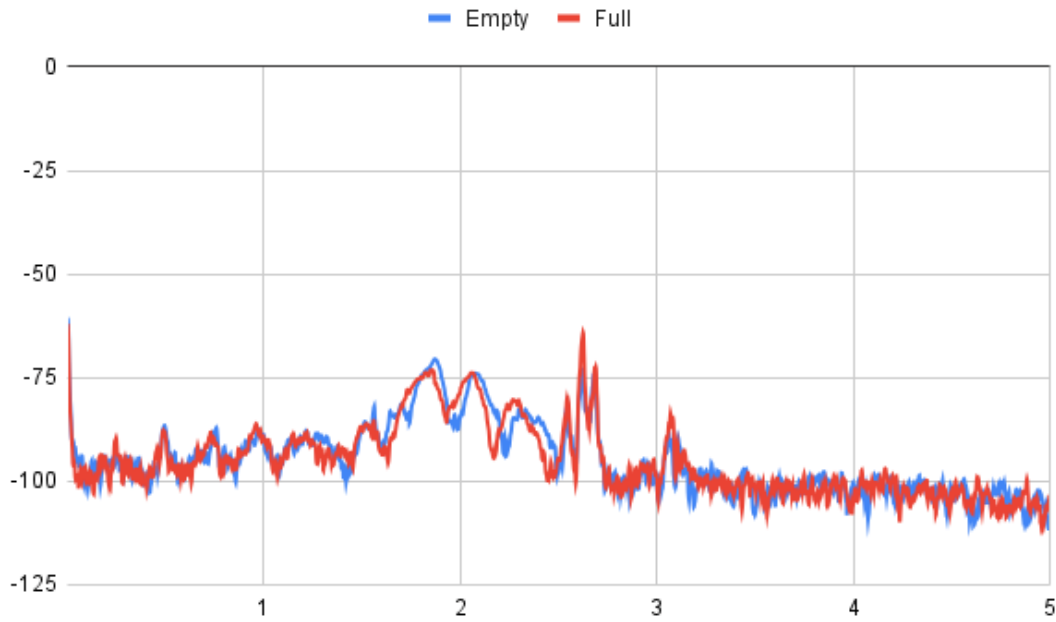


Figure 30: Measurements from experiments with the human body. The blue line shows the measurements post-voiding, and the red line shows the measurements pre-voiding.

4.3 Simulations

[Figure 31](#) shows the results from simulating with the setup showed in [Figure 11](#). The graph is of the $S(2,1)$ parameter which shows the power transfer from transmitting to receiving antenna. The graph shows full and empty phantom model compared to no target at all.

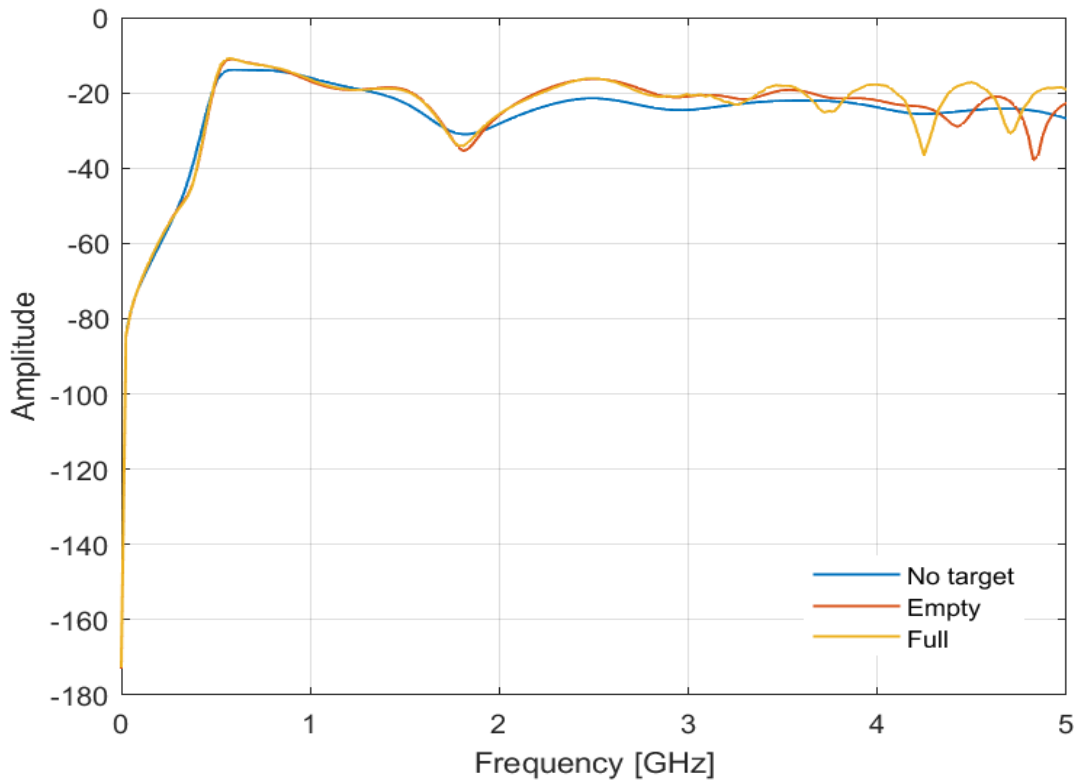


Figure 31: $S(2,1)$ from simulations in EMPro with the setup using the pulse and phantom model used in real-life experiments. The graph includes full and empty bladder as well as no target.

[Figure 32](#) shows the simulated S-parameters for the full and empty bladder with a gaussian first derivative pulse with a pulse width of 0.25 ns.

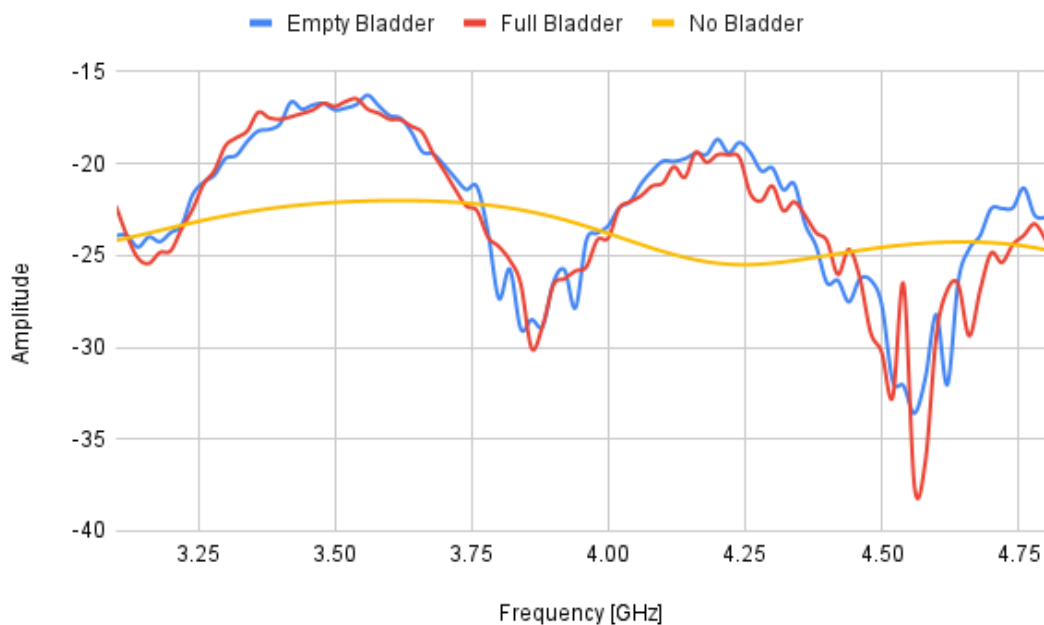


Figure 32: Results from the simulations with a phantom torso. The red line is with a full bladder, the blue line is with an empty bladder, and the yellow line is without any target in front of the antennas.

[Figure 33](#) shows the normalized difference between the full and empty bladders. This is achieved by subtracting the empty and full bladder values, respectively, from the base case of no bladder and plotting their absolute values.

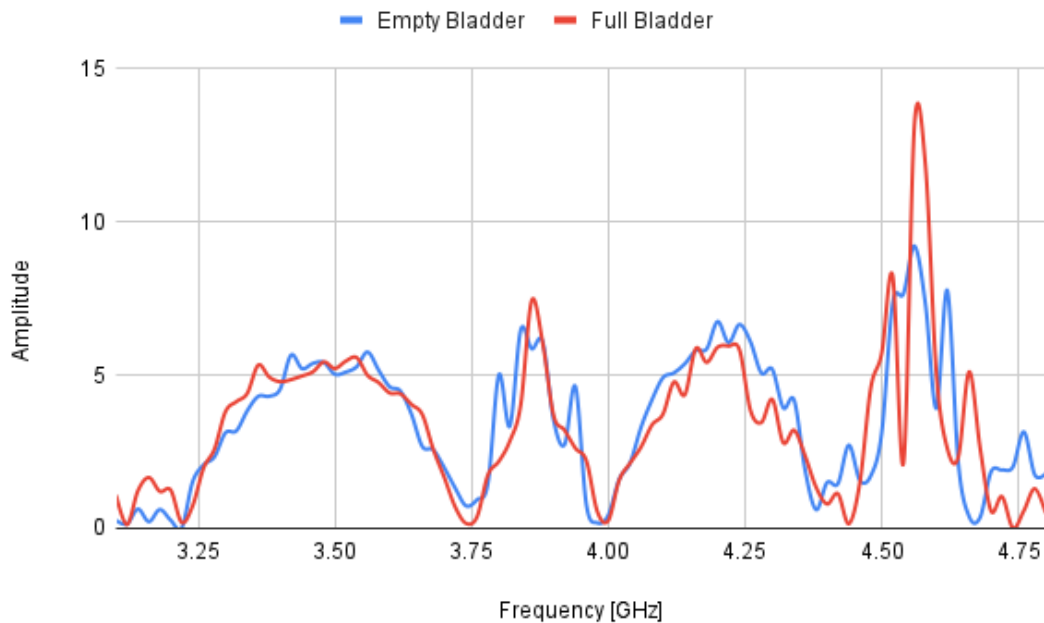


Figure 33: Absolute value of the difference between full and empty bladder.

[Figure 34](#) shows the difference in the placement of the antennas. The blue graph is with the transmitting antenna at one side of the target and the receiving antenna on the other side. The red graph is with both antennas at one side, parallel to each other.

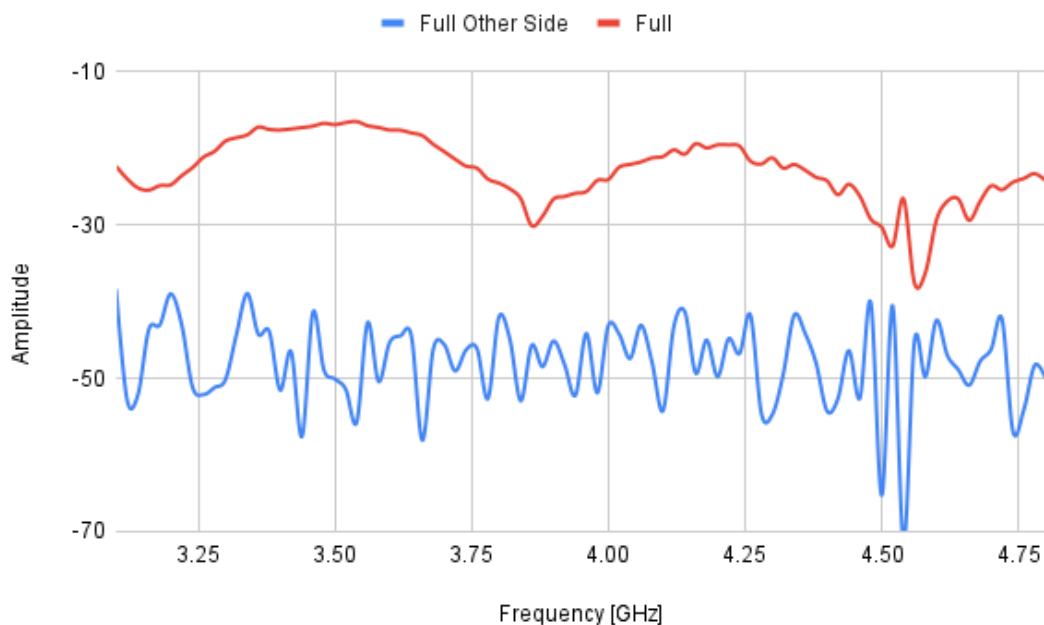


Figure 34: Results from simulations of the full bladder; the red graph shows the results from having the antennas parallel to each other, and the blue graph shows the result from having them on opposite sides of the body.

[Figure 35](#) depicts the distance sweep of the antennas, where they move further away from each other, ranging from 4 cm to 10 cm (4 cm is the closest the antennas can come in real life with the 3D printed attachments). The expected behaviour is confirmed as the coupling between the antennas decreases along with the distance between them.

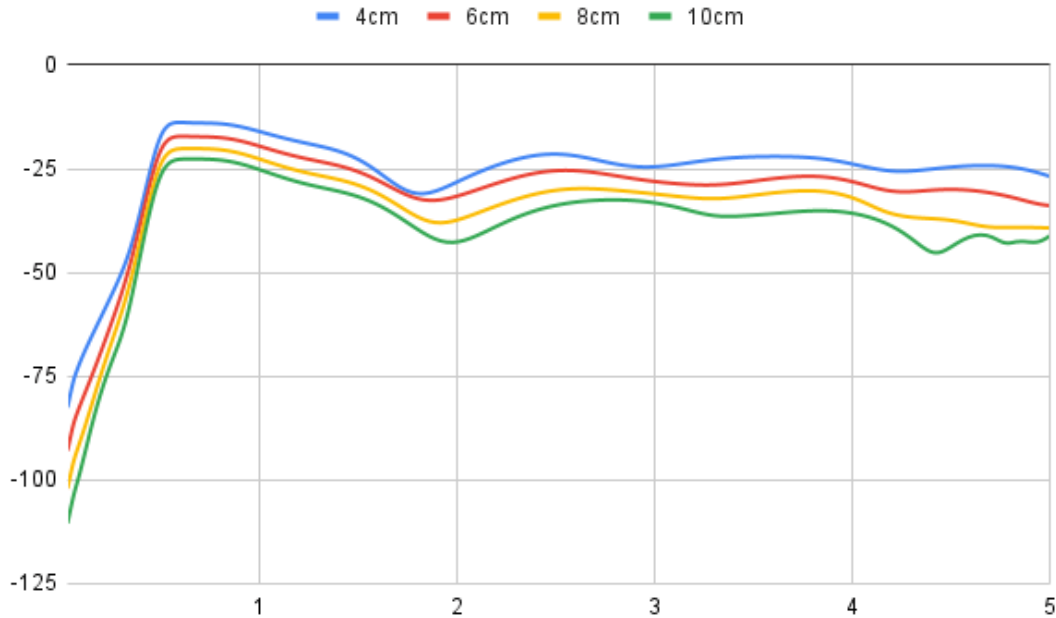


Figure 35: Simulations of different distances between the transmitting and receiving antenna. The transmitting antenna transmits the pulse generated by the pulse generated, which is imported to EMPro, it is a square wave with a pulse width of 10 ns.

5 Discussion

5.1 Antenna

The goals for the antenna design set in this thesis are as follows:

- VSWR should be lower than 2
- The radiation pattern should be directional
- It should have wideband radiation
- The operating frequency should be the permitted frequency range of 3.1 - 4.8 GHz

The antenna meets all four requirements: directional, wideband, and with a VSWR under 2 for the frequencies 3.1-4.8 GHz, both in simulations and reality. Ideally, the VSWR should be 1, meaning the antenna is perfectly matched and the voltage does not vary. However, the overall design is appropriate for this thesis and satisfies the goals.

The far-field radiation pattern shown in [Figure 22](#) shows the simulated radiated power in different directions, and [Figure 23](#) shows the measured radiation pattern. Both are directional and have a similar pattern, except that the simulations show slightly smaller sidelobes. A well-designed directional antenna should have a well-defined main lobe with solid intensity and small side- and back lobes. In our case, the antenna's directionality decreases as we go further away from the center frequency, which can be seen through a weaker main lobe and stronger side and back lobes, indicating a good directionality in both simulations and in measurements taken in the anechoic chamber. The first research question discusses whether the antenna has the potential to measure the reflections from the bladder walls, and the results presented in [4.1 Antenna design](#) shows that it satisfies all parameters to do it properly and in accordance with the PTS regulations.

The low-frequency range results in a larger antenna, as the length of the antenna should be at least one wavelength of the lowest operating frequency. The long wavelength also results in a far-field region further away from the antennas (290.13 mm), resulting in a longer distance between the target and the antennas. For a future product, this is not ideal as a final product should be as small and practical as possible to be portable and designed for everyday usage. However, this thesis only tests the theory and does not produce a complete product.

5.2 Radar

In [4.2 Radar](#), [Figure 28](#) shows that at the lower frequencies where the pulse have most frequency components, the empty phantom model is higher in amplitude than the noise floor (no transmitting pulse), and the full phantom model is slightly higher than the empty one, indicating that it is possible to see a difference, although the differences are small. If the antenna operated in these frequencies, the differences could potentially be more significant. The simulations shown in [4.3 Simulations](#) also prove that it is possible to see a difference between full and empty bladder, both with a pulse width of 10 ns and 0.25 ns. Although, the theory needs to be tested in a real situation with background noise and a more complex target (the human body) to see if the pulse with a pulse width of 0.25 ns can see the difference between a full and an empty bladder.

The radar meets the requirements set by PTS, the frequency range is only acceptable to use if the time for all transmitted signals does not exceed 5% of the time every second and 0.5% of the time every hour. According to the calculations in [3.5 Radar design](#) that uses [Eq. \(9\)\(9\)](#), the duty cycle is well below the PTS limit.

The wavelength of the incident wave and the thickness of the layer which it penetrates determines the magnitude of the reflection. If the layer is the same size or a multiple of the wavelength, a stronger reflection can occur as the reflected waves can align in phase and reinforce each other, i.e., constructive interference could happen. If the layer is thinner or not a multiple of the wavelength, destructive interference could occur instead, making the reflection weaker. The pulse with a pulse width of 10 ns has low-frequency content and, therefore, longer wavelengths, which could cause out-of-phase reflections that give destructive interference.

To begin with, the experiments are not compliant with the expected data because of the pulse width. The pulse generator provided has a minimum pulse width of 10 ns. The desired pulse generator that can transmit shorter pulses was not delivered on time. The experiments were performed, nonetheless, and as expected, the measurements presented in [4.2 Radar](#) did not show any difference between full and empty bladder. The reason is that the pulse generator does not produce a short enough pulse for this application. The range resolution of 1.5 m is not appropriate since the investigated area contains many different objects, and the object of interest is, at its largest, approximately a tenth of the range resolution in length (0.15 m).

An appropriate pulse width and pulse shape must consider the antenna operating frequencies. The frequency response of the pulse spreads over the frequency domain, and it has side lobes with lower amplitude than the main lobe. The pulse with a pulse width of 10 ns has a main lobe outside the frequency range in which the antenna operates most efficiently, and the mismatch between antenna bandwidth and pulse frequency response results in a weak received signal. [Figure 28](#) shows that the signal's sidelobes' amplitudes decrease rapidly as the frequency increases. As the

pulse weakens, the received signal from the antenna weakens as well, and in the frequencies 3.1-4.8 GHz, the received signals converge. If the antennas could properly transmit and receive the pulse, then the pulse should be visible in the time domain of the received signal.

To conclude, the simulations with the phantom model and the pulse used in real-life setup are done to compare with the experiments as they are as close to each other as possible. The simulations with the simple model of a human abdomen and a gaussian first derivative pulse with a pulse width of 0.25 ns are done to verify that another pulse has the potential to see the difference more properly and possibly see the posterior and anterior bladder walls of a human bladder.

5.3 Addressing the research questions

Is it possible to see a difference between empty and full bladder using the antenna designed and fabricated in this thesis and while following the PTS regulations?

The results presented in [Figure 30](#) shows that the human body is too complex to see a difference with the radar setup used in this thesis. The simulations using the simple human abdomen model and with a gaussian first derivative 0.25 ns pulse show a difference and indicate that it is possible with a shorter pulse. However, it is necessary to perform experiments with this pulse in a real-life setup to determine if it is possible.

To conclude, according to the simulations presented in [4.3 Simulations](#), the antennas fabricated in this thesis can adequately detect the reflections from the different boundaries in a simulation environment ([Figure 33](#)), and they can see a difference between full and empty bladder with the 10 ns pulse in the frequency range where the pulse has frequency content ([Figure 28](#)). However, the antennas cannot see the reflections from the posterior and anterior walls of the human bladder in the experiments, as the results in [4.2 Radar](#) show; the reason is further explained in [5.2 Radar](#).

What is the optimal positioning of the transmitting and receiving antennas and their optimal distance to the target for accurate detection?

The antennas are directional and need to be pointed in the direction of the bladder for maximal gain, which can be seen in [Figure 23](#), which shows the radiation pattern. An essential factor to consider is ensuring the antennas are not rotated towards each other, as it will increase the amount radiated directly to the receiver and can overshadow the reflected signals. Because of these considerations, the optimal direction for the antennas is to face the bladder while being parallel to each other. The electric field created by the antennas also affects each other, called coupling. The simulation results in [Figure 35](#) show that the coupling decreases significantly as the

distance increases. However, as the simulated bladder size is 10 cm in diameter for the full bladder and the empty bladder is 6 cm in diameter, the distance should be smaller than 6 cm to uphold the previous criteria regarding directionality and rotation. [Figure 29](#) also shows that in a real-life setup, the coupling is minimal when surrounded by background noise.

Another placement of the antennas has been simulated where they are on opposite sides of the torso, and the results in [Figure 34](#) show that the received reflection strength is almost 1000 times lower than when the antennas are on the same side and parallel to each other. Although, this positioning could be further explored as our simulations have only briefly tested it.

To conclude, the antennas should be parallel and separated by 4 cm to be within the size of the bladder. The optimal distance to the target is 30 cm as that is where the far-field region begins, and therefore the closest the antennas can come to the target, as [3.6 Experiments](#) show and [5.1 Antenna](#) discusses. The separation of the antennas does not need to be several wavelengths as the antennas are directional, and their gain is low on the sides. Some coupling occurs between them, although as [Figure 29](#) shows, it is minimal in a real-life setup contrary to what the simulations in [Figure 35](#) shows where there is no background noise.

How will full 3D simulations of the bladder compare to the experimental data?

When comparing the simulations and the experiments, it is possible to see that the receiving antenna changes in power transfer ([Figure 31](#)); the $S(2,1)$ parameter alters when the phantom model is full even though the pulse is lower in frequency than where the antennas optimally work. Furthermore, as [Figure 28](#) shows, the experiments with a pulse width of 10 ns show a slight difference between the full and empty bladder.

The simulations shown in [Figure 32](#) that use a gaussian first derivative pulse with pulse width of 0.25 ns show a greater difference. As [3.4 Simulations in EMPro](#) shows and [5.4 Further works](#) further explains, a gaussian first derivative with a pulse width of 0.25 ns is more optimal for the antenna and when detecting a smaller target such as the phantom model and the bladder in the human body.

5.4 Further works

Further work is primarily to perform the experiments with a different pulse than the one used in this thesis, e.g., the pulse used in the simulations. The Vivaldi antenna in this thesis ranges from 3.1-4.8 GHz, and a gaussian derivative pulse with a pulse width of 0.25 ns centers at approximately 3.95 GHz. According to [Eq. \(1\)](#), for a 0.25 ns pulse, the range resolution is 3.75 cm which is sufficient when locating the human bladder.

Furthermore, a shorter pulse gives a broader main lobe, and a pulse with 0.25 ns pulse width has a frequency response in the antenna's frequency range ([Figure 13](#)). However, the antenna is not wide enough to cover the entire main lobe, at least not optimally. If the antenna were designed in accordance with FCC regulations (3.1-10.6 GHz), it would cover the entire pulse. However, this thesis aims to follow the PTS regulations, and then the frequency response should also be aligned with the PTS mask; it should be lower than the power spectral density limits for the specific frequency ranges. However, this thesis' antennas are designed per PTS, and the transmitting antenna attenuates the signal in the restricted frequencies (4.8-6 GHz).

Another way to get a shorter pulse is with a pulse generator circuit based on an avalanche transistor, since pulse generators of similar capabilities are quite expensive and hard to come by. A circuit could be designed based on the paper by Guo and Zhu where a square wave with a pulse width of 356 ps is produced [28]. The advantages of using a similar circuit would be easy access to the pulse, portability, and inexpensiveness compared to a pulse generator unit. The EIRP should also be investigated to ensure that it follows the regulations of PTS; the pulse shape and width combined with transmitted power should not exceed the limits.

If another pulse can show two distinctive peaks at the anterior and posterior bladder walls, [Eq. \(10\)\(10\)](#) can describe the distance between them and an algorithm can potentially determine the size of the bladder. Further works should also measure on the human body with a shorter pulse as this thesis first intended to do.

This thesis only uses benchtop equipment and does not consider practical usage. Further work could be to design the system with a final product in regard, taking size and comfort into account.

5.5 Social aspect

The central aspect of this thesis is to improve healthcare regarding bladder monitoring. The UWB radar offers a more comfortable and convenient option than existing options, such as a catheter and ultrasound. It also enables more accurate diagnoses from data gathering, which can lead to a personalized treatment plan. Individuals with bladder-related conditions can effectively control everyday life by having a reliable and non-invasive method of monitoring the bladder, initiating peace of mind and independence. The solution can potentially improve millions of people's quality of life. Furthermore, advances in bladder monitoring using UWB radars show the possibility of using and progressing the technology in other medical applications such as cancer detection.

On the other hand, monitoring and tracking a part of the human body may become an issue of privacy concerns. Data regarding health is sensitive and could be a reason for doubt in the technology.

The environmental aspect of the project highlights that the UWB radar is a reusable piece of equipment compared to the catheter. However, the catheter does not require a power source, making it reliable and energy efficient. Although the UWB radar is reusable and does not create waste after each use, it introduces E-waste, which is harder to recycle and properly dispose of [29]. The lifespan must be weighed against the impact of manufacturing and recycling to fully determine its environmental impact. The enhancement of life quality and healthcare could outweigh the environmental disadvantages.

6 Conclusions

This thesis has tested and evaluated the possibilities of using UWB to monitor the bladder while considering the regulations by Post- och Telestyrelsen. The regulations are more limited than the ones stated by FCC (which accounts for applications in America), and previous works only consider these. The antennas specifically made for this thesis satisfy all the predetermined requirements and they performed according to expectations in both simulations and real-life usage. The performance of the antennas along with the simulations in EMPro show the possibility to use the antennas for bladder state monitoring with ultra-wideband radar and in accordance with the PTS regulations.

This possibility should be further explored with proper equipment, specifically a pulse source that satisfies the technical requirements of the radar system as well as the PTS regulations.

Bibliography

- [1] “Risks of a urinary catheter - NHS.”
<https://www.nhs.uk/conditions/urinary-catheters/risks/> (accessed Feb. 22, 2023).
- [2] H. G. Jo *et al.*, “Forward-looking ultrasound wearable scanner system for estimation of urinary bladder volume,” *Sensors*, vol. 21, no. 16, Aug. 2021, doi: 10.3390/S21165445.
- [3] C. D. Nikolopoulos, A. T. Baklezos, and C. N. Capsalis, “Auto Reconfigurable Patch Antenna for Biomedical Single Channel Multi-Frequency Microwave Radiometry Applications,” 2014.
- [4] B. Borja, J. A. Tirado, and H. Jardón, “An Overview of UWB Antennas for Microwave Imaging Systems for Cancer Detection Purposes,” *Progress In Electromagnetics Research B*, vol. 80, pp. 173–198, 2018.
- [5] M. O’Halloran, F. Morgan, M. Glavin, E. Jones, R. C. Conceio, and D. Byrne, “Bladder-State Monitoring using Ultra Wideband Radar,” *2013 7th European Conference on Antennas and Propagation (EuCAP)*, 2013, Accessed: Feb. 22, 2023. [Online]. Available: <http://ebn.bmj.com/content/4/1/26.short>
- [6] X. Li, E. Pancera, L. Zwirello, H. Wu, and T. Zwick, “Ultra Wideband Radar for Water Detection in the Human Body,” *German Microwave Conference Digest of Papers*, 2010.
- [7] J. Pan, “Medical Applications of Ultra-WideBand (UWB),” 2007.
- [8] “Post- och telestyrelsens författningssamling”.
- [9] I. T. Nassar and T. M. Weller, “A Novel Method for Improving Antipodal Vivaldi Antenna Performance,” *IEEE Trans Antennas Propag*, vol. 63, no. 7, pp. 3321–3324, Jul. 2015, doi: 10.1109/TAP.2015.2429749.
- [10] Y. Zehforoosh, C. Ghobadi, and J. Nourinia, “Antenna Design for Ultra Wideband Application Using a New Multilayer Structure ,” *PIERS ONLINE*, vol. 2, no. 6, 2006, doi: 10.2529/PIERS060531145356.
- [11] K. Holmes-Martin, M. Zhu, S. Xiao, and F. A. Hassani, “Advances in Assistive Electronic Device Solutions for Urology,” *Micromachines 2022*, Vol. 13, Page 551, vol. 13, no. 4, p. 551, Mar. 2022, doi: 10.3390/MI13040551.
- [12] Y. Rahayu, T. A. Rahman, R. Ngah, and P. S. Hall, “Ultra wideband technology and its applications,” *5th IEEE and IFIP International Conference on Wireless and Optical Communications Networks, WOCN 2008*, 2008, doi: 10.1109/WOCN.2008.4542537.
- [13] A. T. Paulose, “HIGH RADAR RANGE RESOLUTION WITH THE STEP FREQUENCY WAVEFORM,” Berkeley, 1988.
- [14] S. Gabriel, R. W. Lau, and C. Gabriel, “The dielectric properties of biological tissues: II. Measurements in the frequency range 10 Hz to 20

- GHz," *Phys Med Biol*, vol. 41, no. 11, p. 2251, Nov. 1996, doi: 10.1088/0031-9155/41/11/002.
- [15] M. E. Bialkowski and Y. Wang, "A size-reduced exponentially tapered slot antenna with corrugations for directivity improvement," *APMC 2009 - Asia Pacific Microwave Conference 2009*, pp. 2482–2485, 2009, doi: 10.1109/APMC.2009.5385343.
- [16] K. Sigfrid Yngvesson, T. L. Korzeniowski, Y. Kim, E. L. Kollberg Senior Member, and J. F. Johansson, "The Tapered Slot Antenna-A New Integrated Element for Millimeter-Wave Applications," vol. 37, no. 2, 1989, doi: 10.1109/22.20062.
- [17] P. J. Gibson, "THE VIVALDI AERIAL," *Conference Proceedings - European Microwave Conference*, pp. 101–105, 1979, doi: 10.1109/EUMA.1979.332681.
- [18] H. Zhang, "Microwave imaging for ultra-wideband antenna based cancer detection," Jun. 2015, Accessed: Mar. 04, 2023. [Online]. Available: <https://era.ed.ac.uk/handle/1842/9958>
- [19] M. M. Rana, R. Khanom, and M. M. Rahman, "Design and Analysis of Vivaldi Antennas," *2018 International Conference on Innovation in Engineering and Technology, ICIET 2018*, Mar. 2019, doi: 10.1109/CIET.2018.8660793.
- [20] D. A. Burrell and J. T. Aberle, "Characterization of Vivaldi antennas utilizing a microstrip-to-slotline transition," *AP-S International Symposium (Digest) (IEEE Antennas and Propagation Society)*, vol. 3, pp. 1212–1215, 1993, doi: 10.1109/APS.1993.385130.
- [21] "PathWave Advanced Design System (ADS)." Keysight Technologies.
- [22] "Momentum PathWave Advanced Design System 2023 Update 1.0." Keysight Technologies. [Online]. Available: <https://edadocs.software.keysight.com/display/engdoc/Notice>
- [23] Keysight Technologies, "EMPro FEM Simulation," 2010. [Online]. Available: <http://www.intel.com/software/products/mkl>
- [24] "FEM Simulation PathWave EM Design 2023 Notices," *Technologies, Keysight*. Keysight Technologies. [Online]. Available: <https://edadocs.software.keysight.com/display/engdoc/Notice>
- [25] "Fast Fourier transform - MATLAB fft - MathWorks Nordic." <https://se.mathworks.com/help/matlab/ref/fft.html> (accessed May 16, 2023).
- [26] Würth Elektronik, "SMA PCB End Launch Jack Flat Tab for 1.6mm PCB WR-SMA," *60312202114514 Datasheet*. May 24, 2018. [Online]. Available: www.we-online.com
- [27] Keysight Technologies, "E8267D PSG Vector Signal Generator."
- [28] Y. Guo and G. Zhu, "Novel design and implementation of ultra-wideband pulse generator based on avalanche transistor." [Online]. Available: <https://www.researchgate.net/publication/289741842>

- [29] Sverige. Naturvårdsverket. and CM gruppen), *Recycling and disposal of electronic waste : health hazards and environmental impacts*. Naturvårdsverket, 2011.